A Quantitative Assessment of Precipitation Associated With the ITCZ in the CMIP5 GCM Simulations

Ryan E. Stanfield(1), Jonathan H. Jiang(2), Xiquan Dong*(1), Baike Xi(1), Hui Su(2),
Leo Donner(3), Leon Rotstayn(4), Tongwen Wu(5), Jason Cole(6), Eiki Shindo(7)

(1) Department of Atmospheric Sciences, University of North Dakota, Grand Forks, ND, USA.
(2) Jet Propulsion Laboratory, Pasadena, CA, USA.
(3) Geophysical Fluid Dynamics Laboratory, Princeton, New Jersey, USA.
(4) Commonwealth Scientific and Industrial Research Organization, Clayton South, Victoria, Australia.
(5) Beijing Climate Center, China Meteorological Administration, Beijing, China.
(6) Canadian Centre for Climate Modeling and Analysis, Environment Canada, Toronto, Ontario, Canada.
(7) Meteorological Research Institute, Japan Meteorological Agency, Tsukuba, Japan.

Final Revision of < CLDY-D-15-00328> to Clim. Dyn. (11/24/ 2015)

* Corresponding author address: Dr. Xiquan Dong, The Department of Atmospheric Sciences,
University of North Dakota, 4149 University Ave. Stop 9006, Grand Forks, ND 58202-9006.
Email: dong@aero.und.edu; Phone: 701-777-6991

Abstract: According to the Intergovernmental Panel on Climate Change (IPCC) 5th Assessment Report (AR5), the broad-scale features of precipitation as simulated by Phase 5 of the Coupled Model Intercomparison Project (CMIP5) are in modest agreement with observations, however, large systematic errors are found in the Tropics. In this study, a new algorithm has been developed to define the North Pacific Intertropical Convergence Zone (ITCZ) through several metrics, including: the centerline position of the ITCZ, the width of the ITCZ, and the magnitude of precipitation along the defined ITCZ. These metrics provide a quantitative analysis of precipitation associated with the ITCZ over the equatorial northern Pacific. Results from 29 CMIP5 Atmospheric Model Intercomparison Project (AMIP) Global Circulation Model (GCM) runs are compared with Global Precipitation Climatology Project (GPCP) and Tropical Rainfall Measuring Mission (TRMM) observations. Similarities and differences between the GCM simulations and observations are analyzed with the intent of quantifying magnitude-, location-, and width-based biases within the GCMs. Comparisons show that most of the GCMs tend to simulate a stronger, wider ITCZ shifted slightly northward compared to the ITCZ in GPCP and TRMM observations. Comparisons of CMIP and AMIP simulated precipitation using like-models were found to be nearly equally distributed, with roughly half of GCMs showing an increase (decrease) in precipitation when coupled (decoupled) from their respective ocean model. Further study is warranted to understand these differences.

1. Introduction

As described in chapter 9 of the Intergovernmental Panel on Climate Change (IPCC) 5th Assessment Report (AR5) (Flato et al. 2013), the majority of the global circulation models (GCMs) underestimate the sensitivity of extreme precipitation to temperature variability or trends, especially in the tropics, which implies that the models may underestimate the projected increase in extreme precipitation in the future. Kendon et al. (2014) studied the intensification of extremes with climate change on a regional scale, over the United Kingdom using a model generally used for weather forecasting with a grid spacing of 1.5 km. Kendon et al. (2014) found that a warmer climate produced an increase in winter hourly rainfall intensities and an increase in high-intensity summer precipitation events indicative of flash flooding. To understand how future climate change might impact precipitation at various scales, it is imperative for us to accurately simulate and predict past and present precipitation.

The treatment of clouds and precipitation in climate models and their associated feedbacks have long been one of the largest sources of uncertainty in predicting any potential future climate changes. Although many improvements have been made in Phase 5 of the Coupled Model Intercomparison Project (CMIP5) (Lauer and Hamilton 2012; Wang and Su 2012; Li et al. 2013; Klein et al. 2013; and Chen et al. 2013), clouds, precipitation, and their feedbacks are still a problem in climate models as concluded in the IPCC AR5 (2013), and illustrated in many studies (e.g., Jiang et al. 2012; Stanfield et al. 2014 and 2015; Dolinar et al. 2015a&b). Many studies (e.g., Stanfield et al. 2014 and 2015, Dolinar et al. 2015a&b) have shown that modeled clouds, radiation, and precipitation, agree with observations within a certain range on a global scale, however, large biases occur at the regional scale. For example, Dolinar et al. (2015b) compared five reanalyzed precipitation rates (PRs) with PRs from the Tropical

Rainfall Measurement Mission (TRMM) and found that the reanalyzed PRs agree with large-scale TRMM mean (3.0 mm/day) to within 0.1–0.6 mm/day, however, the reanalyses oversimulate PRs in both ascent and descent regimes. In particular, the observed and reanalyzed PRs over the ascent regime are an order of magnitude larger than those over the descent regime, indicating different types of clouds exist in these two regimes.

The intertropical convergence zone (ITCZ), a narrow east-west band of vigorous cumulonimbus convection and heavy precipitation (Holton et al. 1971), is located in the ascent regime. In addition to the traditional North Pacific ITCZ, a well-known secondary ITCZ is often found in the southern tropics of many GCMs when they are coupled with their respective ocean model, resulting in a "double-ITCZ" and excessive precipitation in zones south of the equator in the Atlantic and the Eastern Pacific (Lin 2007; Pincus et al. 2008). The double-ITCZ has been a long standing problem within the GCMs. Hirota et al. (2011) examined precipitation in many CMIP3 models and found that models with low skills scores, as defined by Taylor et al. (2001), tended to have a stronger correlation with sea surface temperatures (SSTs), a weaker correlation with vertical motion (ω500), and tended to overestimate (underestimate) precipitation over large-scale subsidence (ascending) regions when compared to models with higher skill scores. Other studies have also examined the interaction of the ITCZ and the equatorial Pacific cold tongue bias in the models (Misra et al. 2008, Li and Xie 2014). In this study, we will focus on the traditional North Pacific ITCZ.

The goal of this study is to provide an accurate assessment of regional precipitation simulated by the AMIP (Atmosphere Model Intercomparison Project) GCM experiment under the Earth System Grid Federation (ESGF) Program for Climate Model Diagnosis and Intercomparison (PCMDI; Taylor et al. 2012). AMIP simulation runs use prescribed sea-surface temperatures, which eliminate potential biases caused by the coupled ocean models of the GCMs. Precipitation from 29 GCM AMIP simulations were thoroughly compared with the GPCP (Adler et al. 2003) and TRMM (Huffman and Bolvin, 2011) observations, as well as with their linked CMIP5 historical ocean-coupled runs. In this study, an algorithm has been developed to define the North Pacific ITCZ through several metrics with the intent of quantifying magnitude-, location-, and width-based biases within the GCMs**.** The ITCZ is a major feature component of the global circulation, and serves as a good metric for testing the GCMs.

2. Data

In this study, precipitation from 29 AMIP simulations were compared with GPCP and TRMM observations, and to their CMIP historical counterparts where available. For our comparison, all data are interpolated to a specific 1° × 1° (latitude × longitude) grid using bilinear interpolation. In order to account for the varied spatial resolutions of the GCMs (Table 1), as well as smoothing biases generated from our interpolations, GPCP and TRMM observations undergo two interpolations. The observations are first interpolated from their original resolutions to match the spatial grid of each respective GCM, and then the observations are interpolated a second time to the shared 1° × 1° grid for comparison. All data were downloaded from the ESGF PCMDI database for the period of January 2000 to December 2005, providing six full years of monthly data. This timeframe was chosen due to data availability as well as an effort to reduce the influence of the El Niño Southern Oscillation (ENSO), as it was found that this timeframe maintained a weak to moderate strength in the ENSO. Like months (e.g. all “January” months, etc.) are averaged together to generate the monthly means shown in this study.

a. CMIP5 AMIP and Historic GCM Simulations

This study compares the precipitation products from 29 AMIP GCM simulations with prescribed SSTs, which are available from the ESGF PCMDI database (Taylor et al. 2012). Each ensemble member within the ESGF PCMDI database is given three integers (N,M,L), in r<N>i<M>p<L> format to distinguish related simulations, where N is the realization number, M is the initialization method indicator, and L is the perturbed physics number as described in Taylor et al. (2010). Monthly data from each respective r1i1p1 GCM simulation is used in this study. In section 3c, historical ocean-coupled simulations are paired with AMIP simulations as outlined in Table 1.

b. GPCP

The Global Precipitation Climatology Project (GPCP, Adler et al. 2003) is part of the Global Energy and Water Cycle Exchanges Project (GEWEX) established by the World Climate Research Programme (WCRP). The GPCP product used in this study is the GPCP satellite-gauge (SG) monthly precipitation product, which provides monthly precipitation estimates on a global 2.5°×2.5° grid based on a combination of data from geostationary satellites, polar satellites, surface reference data, and station observations. Uncertainty of precipitation in the GPCP-SG product is estimated at ~15% (Huffman et al. 1997).

c. TRMM

The Tropical Rainfall Measuring Mission (TRMM, Huffman and Bolvin 2011) precipitation product is generated through a combination of four sources: the TRMM precipitation radar data, passive microwave radiances at multiple frequencies and polarizations (observed from a mixed constellation of operational and research low-earth-orbit [LEO] satellites), thermal infrared brightness temperatures from geosynchronous satellites, and surface precipitation gauge measurements (Huffman et al. 2007; Huffman and Bolvin 2011). This study uses the 3B43 monthly TRMM dataset with a native resolution of 0.25° × 0.25° (latitude × longitude). The TRMM microwave imager is available between ±37° of latitude. An important difference between the GPCP and TRMM products is the inclusion of the precipitation radar on-board the TRMM satellite. Given the higher spatial resolution and ability of the precipitation radar to detect precipitating clouds, we expect the precipitation features identified by TRMM to be finer/sharper than features identified by GPCP.

The uncertainties of 3-hourly TRMM precipitation data are estimated at 90% - 120% for light rain (< 0.25 mm/hr) and 20% - 40% for heavy rain (Habib and Krajewski 2002; AghaKouchak et al. 2009). Some of the uncertainties in the TRMM data are considered to be randomly scattered errors, which can be significantly reduced when averaged over space and time. However, TRMM data is also known to have up to a ~30% positive bias during the northern summer when compared to other measurements (e.g. Nicholson et al. 2003), which cannot be removed through monthly averaging. It should be noted that at the time of this study, generation of the GPCP product does not include TRMM observations (Huffman and Bolvin, 2012).

3. Methodology

a. Defining the Area of Focus (AOF)

In the IPCC AR5, it was concluded that the GCMs in CMIP5 contain systematic errors in the Tropics (IPCC AR5 Ch.9; Flato et al. 2013). To examine these systematic errors, we compare the modeled area-weighted mean precipitation within the tropics and subtropics (±40° latitude) with GPCP and TRMM observations (Fig. 1). Figure 1 shows that all 29 of the GCM simulations examined in this study oversimulate precipitation compared to both GPCP and TRMM observations between ±40° of latitude both annually (Fig. 1a) and seasonally (Figs. 1b-c). The annual mean precipitation from the GCM ensemble is ~13% greater than both GPCP and TRMM observations (~3 mm/day), with the GCMs ranging from 3.11 mm/day (IPSL-CM5A) to 3.73 mm/day (INM-CM4). No strong seasonal variation is observed as shown in Figs. 1b and 1c.

Comparisons of annual mean precipitation between the GPCP, TRMM, and the GCM ensemble over ±40° latitude for the 6-yr study period are shown in Fig. 2. This comparison shows that the mean precipitation simulated by the ensemble of GCMs (Fig. 2c) is higher than both GPCP (Fig. 2a) and TRMM (Fig. 2b) observations, particularly in regions of large-scale ascent such as the North Pacific ITCZ.

To make proper comparisons between the GCM simulations and observations, an area of focus (AOF) has been defined by the boundaries 2° S to 21° N and 180° W to 110° W in this study (green box in Fig. 2). The selected AOF covers the full breadth of the ITCZ across all seasons as demonstrated using GPCP and TRMM observations in Fig. 3. With the AOF defined by these boundaries, we cover most of the precipitation simulated by the GCMs while also limiting exposure to exterior regional biases. These biases include spurious precipitation cells that occur north of the Pacific ITCZ in some GCMs which are strong enough to potentially distract the algorithm from properly identifying the ITCZ as well as potential land effects found outside of the eastern and western edges of the AOF.

b. Defining the ITCZ and ITCZ Metrics

In this study, an algorithm has been developed to analyze and compare the ITCZ simulated by each of the GCMs with collocated observations. The algorithm first outlines the boundaries of the ITCZ, and a variety of metrics are pulled based on these boundaries. An example of output from the algorithm is provided in Fig. 4 using monthly averaged precipitation in January simulated by the Australian ACCESS 1-3 GCM. In detail, the algorithm first attempts to identify the upper and lower boundaries of the ITCZ band (orange lines in Fig. 4) across each degree of longitude within the AOF by identifying the longest continuous stretch of precipitation above a set monthly precipitation rate threshold. The monthly thresholds defined in this study vary by month (4 mm/day from January to June, 6 mm/day from July to December). These thresholds were chosen based on our monthly analysis of TRMM and GPCP observations in the ITCZ. As demonstrated in Fig. 4, these thresholds can be used to clearly identify the boundaries of the ITCZ.

After defining the upper and lower boundaries, a centerline (white line in Fig. 4) is derived as the midpoint between the upper and lower boundaries at each degree of longitude. When no values were found above the precipitation threshold for a given longitude, the algorithm will either interpolate between the nearest two known points of the ITCZ centerline or extrapolate outward by finding the average slope of the nearest 10 points. The width of the ITCZ, here after referred to as width of the band, is defined as the latitude of the upper ITCZ boundary minus the latitude of the lower ITCZ boundary. When all simulated precipitation rates across a set degree of longitude are below the monthly thresholds, a value of zero is given for the width of the ITCZ at that longitude.

All metrics and comparisons in this study are calculated and shown against both collocated GPCP and TRMM observations. The only exception to this in the centerline comparisons, where it was found that the centerlines derived from GPCP and TRMM observations predominately deviated by less than 1° of latitude. Therefore, centerline comparisons are conducted by comparing the GCM derived centerlines against the average of the GPCP and TRMM derived centerlines.

To examine the magnitude of simulated precipitation along the ITCZ, we first calculate the average of all points of precipitation within ±4° latitude of the observed centerline for each GCM. These values are then compared to the average magnitude of precipitation observed from both GPCP and TRMM, which are both calculated as the average of all points of precipitation within ±4° latitude of the averaged observed centerline from each observation. It should again be noted that all observational fields have been interpolated twice; once from their native resolution to the spatial resolution of each GCM grid, and then a second time to convert back to the standardized 1° × 1° (latitude × longitude) grid during comparisons. This was done to provide a better apples-to-apples comparison by minimizing bias due to smoothing. The use of four degrees of latitude was chosen during analysis because using this range covered the full visible width of the observed ITCZ each month.

The overall precipitation bias found between the Pacific ITCZ simulated by each GCM and the ITCZ observed by GPCP and TRMM can generally be expressed as a combination of three partitions. These three partitions are shown in Fig. 5 using idealized distributions of precipitation across a set longitudinal line: positional/locational biases (Fig. 5a), magnitude/intensity biases (Fig. 5b), and biases in the width of the simulated ITCZ (Fig. 5c). The algorithm developed in this study is designed to quantitatively estimate the strengths of these biases. These biases can be attributed to the physical parameterizations and dynamic schemes in different GCMs.

Comparisons have been made between CMIP and AMIP simulations using identical parameterizations in each GCM. It should be noted that while precipitation is a diagnostic property within the GCMs, precipitation has a feedback on the large-scale state, making it difficult to separate the contributions of dynamic schemes and physical parameterizations to precipitation biases.

The methods used to examine and compare the simulated ITCZs in this study were chosen in an attempt to provide the most balanced and fair comparison between all CMIP5 GCMs. When developing the algorithm used in this study, three difficulties had to be overcome to provide a fair comparison: (1) Missing precipitation, (2) non-Gaussian distributions, and (3) spurious cells North of the ITCZ. For example, a few of the models severely undersimulated precipitation in the ITCZ, thus the west-east precipitation field was not continuous across the AOF. In these circumstances, the centerline of the ITCZ had to be estimated using interpolation or extrapolation based on the known centerline locations. While the observations showed a Gaussian-like distribution across a longitudinal line, many of the GCMs exhibited northerly skewed distributions of precipitation. An attempt was made to use an e-folding technique to identify the boundaries of the ITCZ, however, this attempt was unsuccessful because it could not treat all of the GCMs equally and fairly due to the non-Gaussian distributions of precipitation in many of the GCMs. These skewed distributions also limited our ability to use maximum precipitation as a centerline identifier. Many of the GCMs also showed large patches of high precipitation rates north of the ITCZ, which made it difficult to use a percentage-based system to identify the ITCZ boundaries. It is because of these challenges that we have chosen the threshold based method to derive ITCZ metrics.

4. Results and Discussion

The algorithm developed in this study has provided several metrics, allowing us to determine potential strengths of magnitude-, location-, and width-based precipitation biases in the GCMs over the Pacific ITCZ compared to GPCP and TRMM observations. These metrics include the centerline position, the width of the ITCZ, and the magnitude of precipitation along the simulated ITCZ. We quantitatively examine these metrics using observations as the ground truth.

All barplots shown in Figs. 6-9 follow the same overall design. Each month is color coded as shown in the legends. The horizontal black line in each of these figures represents a perfect match with the baseline metric when comparing with the modeled results. The observations are used as a baseline in Figs. 6-8, while CMIP results are used as the baseline in Fig. 9. Monthly values for each of the metrics presented are vertically stacked for each GCM, indicating that monthly values of each metric should be measured as the height of each respective bar for that month only. More specifically, the length of each bar should be compared to the scale length shown on the diagram. Tick marks along the y-axis of match the scale length presented in each figure. To alleviate potential confusion, values on the y-axis of these barplots have been removed, as including values tends to suggest an incorrect cumulative nature.

a. Centerline and Width of the ITCZ in AMIP Simulations

Figure 6 shows the differences in ITCZ centerline position between each GCM simulation and the averaged centerline of GPCP and TRMM observations. Monthly values above (below) the horizontal black line represent months where the modeled ITCZ centerline of the respective GCM was found to simulated more northward (southward) compared to the averaged centerline of GPCP and TRMM observations. Note that monthly values in Fig. 6 are vertically stacked for each GCM, with a tick spacing of 2 degrees.

Figure 6 has demonstrated that most of the GCMs tend to simulate the ITCZ centerlines northward compared to GPCP and TRMM observations, with the greatest shifts occurring in March. While most of the GCMs simulate the ITCZ centerlines northward, it is worth noting that both the Chinese BCC-CSM1-1 and the BCC-CSM1-1-m tend to shift the ITCZ centerlines southward compared to the observed centerline. Some models show promise, with low biases or by a balancing of northward and southward months, such as the ACCESS1-0, ACCESS1-3, CCSM4, CESM-CAM5, CanAM4, HadGem2-A, and the MRI-AGCM3.

Comparisons of the ITCZ widths between each GCM and the GPCP observation are shown in Fig. 7a, while comparisons with the TRMM observation are shown in Fig. 7b. Tick spacing shown in Fig. 7 is 4 degrees. Monthly values above (below) the horizontal black line represent months where the vertical width of the modeled ITCZ is wider (thinner) than the ITCZ observed by GPCP (Fig. 7a) or TRMM (Fig. 7b). Comparing Figs. 3 and 7, we found that the width of the ITCZ observed by TRMM is thinner than the ITCZ observed by GPCP. The thinner band found in the TRMM observations is attributed to two factors: TRMM observations have a finer native resolution, and the TRMM satellite uses the on-board precipitation radar which is able to detect precipitating clouds but is insensitive to non-precipitating clouds, while the GPCP product is primarily derived from satellite infrared brightness measurements where the cloud-top temperatures from precipitating and non-precipitating clouds are almost the same (Stenz et al. 2014, 2015).

Results shown in Fig. 7 show that most of the GCMs simulate a wider band of precipitation (above the horizontal black line) in the Pacific ITCZ compared to both GPCP (Fig. 7a) and TRMM (Fig. 7b) observations. A few of the GCMs simulate the width of the ITCZ relatively close to the ITCZ observed from GPCP, such as the ACCESS1-3, CMCC-CM, IPSL-CM5A-LR, IPSL-CM5A-MR, MPI-ESM-LR, MPI-ESM-MR, and the MRI-AGCM3. However, these models all simulate wider bands of precipitation more frequently when compared to the ITCZ observed from TRMM. The IPSL-CM5B-LR is the only model to simulate a thinner band of precipitation for nearly all months when compared to GPCP and TRMM. It should be noted that the precipitation produced by the IPSL-CM5B-LR drops below the monthly thresholds for large sections of the ITCZ. The differences shown between the French IPSL-CM5A-LR and IPSL-CM5B-LR are hypothesized to be a result of the changes made to parameterizations in the IPSL-CM5B-LR model (Dufresne et al. 2012, Hourdin et al. 2013). Interestingly, the BCC-CSM1-1 and the BCC-CSM1-1-m simulations show opposite results compared to each other in Fig. 7, suggesting either a significant change in modeled dynamics or that differing spatial resolution of these two models may play a role.

b. Magnitude of Precipitation in AMIP Simulations

Comparisons in the magnitude of precipitation between the GCMs and GPCP and TRMM observations are presented in Figs. 8a and 8b, respectively. The tick spacing in Fig. 8 is given as 4 mm/day. Monthly values above (below) the horizontal black line represent months where the magnitude of precipitation in the ITCZ of the GCM is simulated stronger (weaker) than that of the respective observations. It should be noted that the biases in the magnitude of precipitation are prone to both magnitude and positional errors. Comparing GPCP and TRMM observations using the results from Fig. 8a and Fig. 8b shows only minor variations from month to month between the two comparisons.

It is shown in Figs. 8a and 8b that most of the GCMs simulated stronger precipitation compared to both GPCP and TRMM observations. A few models, namely the BCC-CSM1-1 and the suite of IPSL GCMs, simulated less precipitation than both observations. Of the GCMs that were found to be oversimulating precipitation in the Pacific ITCZ, most of these GCMs had higher biases in the northern hemispheric summer months, with June showing the highest positive precipitation bias.

Based on our comparisons in Figs. 6-8, we can conclude that the models tend to simulate a stronger, wider ITCZ shifted slightly northward compared to the ITCZ in GPCP and TRMM observations.

c. Historical/CMIP vs AMIP Simulations

The metrics derived in this study, the ITCZ Centerline, width of the ITCZ band, and precipitation magnitude, are prone to both positional/dynamic and magnitude/parameterization biases. To examine the strength and role of the coupled ocean dynamics/positional biases, we compare historical and AMIP simulations with identical parameterizations. In detail, the precipitation from 20 available historical and AMIP simulations have each been averaged between ±4° latitude of the average observed centerline, and their differences are shown in Fig. 9 given as the historical simulation (CMIP) minus the AMIP simulation. Since the AMIP and

CMIP versions of each models compared in Fig. 9 use the same parameterizations, their precipitation differences are highly attributed to dynamic/positional influences, which can be used to estimate the strength of the potential bias in each GCM. A list is provided in Table 1 to identify how this study has linked the historical and AMIP simulations between GCMs.

In general, the comparisons of precipitation simulated by identical AMIP and CMIP versions of the model are nearly equally distributed around the black line (Fig. 9). More specifically, there is roughly an even split between three different scenarios where: (1) the CMIP version of the GCM simulated more precipitation than their AMIP counterparts (e.g., ACCESS1-3, CMCC-CM, CanAM4, IPSL-CM5, MIRCO5), (2) the CMIP version of the GCM simulated less precipitation than their AMIP counterparts (e.g., ACCESS1-0, BCC-CSM1-1m, CSIRO-MK3-6-0, GFDL-AM3), or (3) the model showed a monthly split between simulating more/less precipitation when comparing CMIP and AMIP simulations (e.g., BCC-CSM1-1, BNU-ESM, FGOAL, NorESM1-M). To investigate their differences, we examined the vertical upwelling (omega, ω) fields at 850 mb and found that there is no significant difference between two simulations. Further study is warranted to understand why some of the CMIP models simulated more precipitation, while others simulated less precipitation compared to their AMIP counterparts. The role of SST during the simulations will be examined.

5. Detailed Analysis of Select Models

In an effort to more thoroughly show the results and differences presented in this study, a more detailed analysis is discussed for seven of the GCMs presented in this study. These models were chosen based on available feedback from these modeling groups, interesting metric results, and their documentation of convective and stratiform parameterizations listed in Table 2. Many of the GCMs were found to have particular patterns during the following specified seasons: northern hemispheric (NH) winter (DJF), NH spring (MAM), NH summer (JJA), NH fall (SON).

The ITCZ simulated by the BCC-CSM1-1 can be characterized across most months as having a very chaotic precipitation pattern and ITCZ width (Fig. 10). Based on the analysis above, the BCC-CSM1-1 shows moderate agreement across all metrics, however monthly analysis of BCC-CSM1-1 results shows a different picture. In the DJF and MAM seasons, simulated precipitation rates are much lower than the set threshold within the western portion of the AOF when compared to the observations, resulting in the algorithm having to resort to using calculated slopes from the eastern portion of the AOF to estimate the position of the ITCZ. Overall, however, the BCC-CSM1-1 still undersimulates precipitation within the eastern portion of the AOF compared to the observations. Because of this, the calculated centerline position and width of the ITCZ jumps drastically from point to point in the winter and spring seasons, balancing in our analysis to show a thin undersimulated band of precipitation.

During the JJA and SON seasons, however, the BCC-CSM1-1 simulated heavy precipitation in the western portion of the AOF, while simultaneously simulating very little precipitation in the eastern portion of the AOF. The oversimulation of precipitation in the west balances with the undersimulation of precipitation in the east, causing the BCC-CSM1-1 to appear much better in annual precipitation comparisons. It should be noted as well, that the algorithm effectively fails when estimating the position of the BCC-CSM1-1 simulated ITCZ in November. The precipitation simulated by the BCC-CSM1-1 in November dropped well below the threshold east of ~140° W, and the algorithm attempted to derive a slope from the known but chaotic precipitation field west of the drop-off. This results in the estimation of the ITCZ well into the southern-hemisphere and causes the algorithm to fail. It should be noted that this is the only time the algorithm was found to incorrectly estimate the ITCZ centerline when precipitation rates dropped below the set threshold for an extended period of time. In summation, the BCC-CSM1-1 shows moderate agreement with GPCP and TRMM observations in the annually based comparisons, however, extensive seasonal analysis has shown that these good agreements are due a balancing of biases in a chaotic precipitation field.

As demonstrated in Figs. 6-9, ITCZ features simulated by the BCC-CSM1-1-m are significantly different compared to its BCC-CSM1-1 counterpart. For example, the widths of the ITCZ simulated by the BCC-CSM1-1-m are larger than the BCC-CSM1-1 across all months. While the width of the ITCZ does vary slightly across the AOF, the variations are far less chaotic than those found in the BCC-CSM1-1. The width of ITCZ simulated by the BCC-CSM1-1-m is the noisiest in November, which correlates with the greatest northward shift of the ITCZ in the BCC-CSM1-1-m. Other than in November, the ITCZ simulated by the BCC-CSM1-1-m is located southward compared to the observations. The significant differences shown between the BCC-CSM1-1 and the BCC-CSM1-1-m are unexpected given that these models use identical convective and stratiform parameterizations. The only difference between these two models, as we know, is that the horizontal resolution of the BCC-CSM1-1-m is much finer compared to BCC-CSM1-1 (Table 1).

ITCZ precipitation simulated by the GFDL-AM3 tends to be shifted slightly northward across all months other than in the JJA season, with the largest shifts found in the SON season. The simulated ITCZ is found to be wider than the observations across all months with the widest band occurring in the SON season, which results in the large shift northward mentioned previously. Precipitation intensity shows to be oversimulated nearly equally across all months compared to GPCP and TRMM observations. The GFDL-HIRAM-C180 (C180) and GFDL-

HIRAM-C360 (C360) simulated widths of the ITCZ are slightly more chaotic than its GFDL-AM3 counterpart. This is hypothesized to be a result of the higher resolutions in the C180 and C360 GCMs. The ITCZ is simulated northward compared to GPCP and TRMM observations in both the C180 and C360 GCMs, with the C180 simulating the ITCZ slightly more northward than the C360. Precipitation intensity and the width of the ITCZ are stronger and wider in the C360 than compared to the C180, while both models simulated wider ITCZs of stronger intensity compared to both GPCP and TRMM observations.

An interesting split is found when comparing the centerline positions simulated by the MRI-AGCM3-2H (2H) and MRI-AGCM3-2S (2S) GCMs (Mizuta et al. 2012, Murakami et al. 2012). Both simulated ITCZs are northward compared to GPCP and TRMM observations, however, the 2H simulation tends to simulate the ITCZ slightly more northward in the DJF months compared to the 2S, while the 2S tends to simulate the ITCZ slightly more northward in the MAM season. Both the 2H and 2S models simulated a slightly wider ITCZ across all months compared to the observations. Comparing the width of the ITCZ in the 2H and 2S GCMs, the 2S tends to have a slightly more chaotic bandwidth, which is again hypothesized to be a result of the higher resolution used in the 2S simulation. Both simulations have higher precipitation rates across all months when compared to the GPCP observations, however, the 2H simulated slightly less precipitation compared to TRMM observations during the DJF season.

All of the discussions in this section are based the results found in this study. It is difficult to identify the physical reasons behind the similarities, differences, and biases of each model without manually running the GCMs and examining each GCM on finer temporal scales. Hopefully, this study will serve as a guide to identify these differences found in the GCM simulations.

6. Summary and Conclusions

In this study, a new algorithm has been developed to define the North Pacific ITCZ through several metrics, including: the centerline position of the ITCZ, the width of the ITCZ, and the magnitude of precipitation along the defined ITCZ. These metrics allow us to quantitatively evaluate magnitude-, location-, and width-based precipitation biases over the Pacific ITCZ from 29 CMIP5 GCMs using the GPCP and TRMM observations as a ground truth. Based on the ITCZ metrics derived from our multiyear analysis and the comparisons between the model simulations and observations, the following conclusions have been made:

1) The GCMs predominately simulate the centerline of the ITCZ northward when compared to GPCP and TRMM observations, with the greatest shifts occurring in March. Very few GCMs shift southward, such as the BCC-CSM1-1 and the BCC-CSM1-1-m. Some of the models show promise, with either low biases or by a balancing of northward and southward biases such as the ACCESS1-0, ACCESS1-3, CCSM4, CESM-CAM5, CanAM4, HadGem2-A, and the MRI-AGCM3.
2) Most of the GCMs simulate a much wider band of precipitation in the Pacific ITCZ compared to both GPCP and TRMM observations. A few of the GCMs simulated ITCZ widths relatively close to the observations, such as the ACCESS1-3, CMCC-CM, IPSL-CM5A-LR, IPSL-CM5A-MR, MPI-ESM-LR, MPI-ESM-MR, and the MRI-AGCM3. The IPSL-CM5B-LR is the only model to generate a thinner band of precipitation.
3) The GCMs tend to oversimulate precipitation compared to GPCP and TRMM observations. Of these GCMs, most have higher biases in the northern hemispheric summer months, with June showing the highest positive precipitation bias. A few of the models, namely the BCC-CSM1-1 and the suite of IPSL GCMs, simulate less precipitation than the observations.

4) Comparisons of precipitation simulated by identical AMIP and CMIP versions of the model are nearly equally distributed for the 20 available GCMs used in this study. In detail, an equal split is found between three scenarios. For some of the GCMs, the CMIP version of the GCM simulated more precipitation than their AMIP counterparts, while in other GCMs their AMIP counterpart simulated more precipitation. Some of the GCMs showed an even split between CMIP or AMIP simulations simulating more precipitation, nearly cancelling out in the net effect. Analysis of vertical upwelling (omega, ω) fields at 850 mb showed no significant difference between two simulations. Further study is warranted to understand why some CMIPs simulated more precipitation, while others were less than their AMIP counterparts.

Acknowledgements

We would like to acknowledge the contributions made by Trond Iversen, for providing information and references on the NorESM model, and the contributions made by Cyril Morcrette, for his comments and suggestions related to HadGEM2-A model. Data were obtained from the CMIP5 ESGF PCMDI database at http://pcmdi9.llnl.gov/esgf-web-fe/. GPCP and TRMM data are also provided by the Obs4MIPS program and are available as well from the ESGF PCMDI database at http://pcmdi9.llnl.gov/esgf-web-fe/. The researchers at University of North Dakota were supported by NASA CERES (NNX14AP84G) and EPSCoR projects, and the researchers at JPL were supported by NASA ROSES12-MAP and ROSE13-NDOA projects. The GPCP SG combined precipitation data were developed and computed at the NASA/Goddard Space Flight Center's Mesoscale Atmospheric Processes Laboratory – Atmospheres as a contribution to the GEWEX Global Precipitation Climatology Project.

References

Adler et al (2003) The Version 2 Global Precipitation Climatology Project (GPCP) Monthly Precipitation Analysis (1979–Present). J. Hydrometeor., 4, 1147–1167.

AghaKouchak A, Nasrollahi N, Habib E (2009) Accounting for Uncertainties of the TRMM Satellite Estimates. Remote Sens., 1, 606-619.

Anderson J et al. (2004) The new GFDL global atmosphere and land model AM2-LM2: Evaluation with prescribed SST simulations. J. Climate, 17, 4641-4673.

Bentsen et al (2013) The Norwegian Earth System Model, NorESM1-M – Part 1: Description and basic evaluation of the physical climate. Geosci. Model Dev., 6, 687–720; doi:10.5194/gmd-6-687-2013

Bretherton CS, McCaa JR, Grenier H (2004) A new parameterization for shallow cumulus convection and its application to marine subtropical cloud-topped boundary layers. Part I: Description and 1D results. Mon. Wea. Rev., 132, 864-882.

Chaboureau JP, Bechtold P (2002) Simple Cloud Parameterization Derived from Cloud Resolving Model Data: Diagnostic and Prognostic Applications. J. Atmos. Sci., 59, 2362-2372.

Chen L, Yu Y, Sun D (2013) Cloud and water vapor feedbacks to the El Niño warming: are they still biased in CMIP5 models? J Clim. doi:10.1175/JCLI-D-12-00575.1

Dolinar E, Dong X, Xi B, Jiang J, Su H (2015a) Evaluation of CMIP5 simulated clouds and TOA radiation budgets using NASA satellite observations. Clim Dyn, 44, 2229-2247. doi:10.1007/s00382-014-2158-9

Dolinar E, Dong X, Xi B (2015b) Evaluation and Intercomparison of Clouds, Precipitation, and Radiation Budgets in Recent Reanalyses using Satellite-Surface Observations. Climate Dynamics, DOI: 10.1007/s00382-015-2693-z.

Donner LJ (1993) A cumulus parameterization including mas fluxes, vertical momentum dynamics, and mesoscale effects. J. Atmos. Sci., 50, 889-906.

Donner LJ, Seman CJ, Hemler RS (2001) A cumulus parameterization including mass fluxes, convective vertical velocities, and mesoscale effects: Thermodynamic and hydrological aspects in a general circulation model. J. Climate, 14, 3444-3463.

Donner LJ et al. (2011) The dynamical core, physical parameterizations, and basic simulation characteristics of the atmospheric component of the GFDL coupled model CM3. J. Climate, 24, 3484-3519, doi: 10.1175/2011JCLI3955.1.

Dufresne et al (2012) Climate change projections using the IPSL-CM5 Earth System Model: from CMIP3 to CMIP5. Clim Dyn, 40, 2123-2165. doi:10.1007/s00382-012-1636-1

Flato G, Marotzke J, B. Abiodun B, Braconnot P, Chou SC, Collins W, Cox P, Driouech F, S. Emori S, V. Eyring V, Forest C, Gleckler P, Guilyardi E, Jakob C, Kattsov V, Reason C, Rummukainen M (2013) Evaluation of Climate Models. In: Climate Change 2013: The Physical Science Basis. Contribution of Working Group I to the Fifth Assessment Report of the Intergovernmental Panel on Climate Change [Stocker, T.F., D. Qin, G.-K. Plattner, M. Tignor, S.K. Allen, J. Boschung, A. Nauels, Y. Xia, V. Bex and P.M. Midgley (eds.)]. Cambridge University Press, Cambridge, United Kingdom and New York, NY, USA.

Gebremichael M, Krajewski WF, Morrissey M, Langerud D, Huffman GJ, Adler R (2003) Error Uncertainty Analysis of GPCP Monthly Rainfall Products: A Data-Based Simulation Study. J. Appl. Meteor., 42, 1837–1848.

Gregory D, Rowntree PR (1990) A mass flux convection scheme with representation of cloud ensemble characteristics and stability-dependent closure. Mon. Weather Rev., 118, 1483-1506.

Gregory D, Allen S (1991) The effect of convective scale downdraughts upon NWP and climate simulations. 9th Conference on Numerical Weather Prediction. American Meteorological Society: Denver, CO; 122-123.

Habib E, Krajewski WF (2002) Uncertainty Analysis of the TRMM Ground-Validation Radar-Rainfall Products: Application to the TEFLUN-B Field Campaign. J. Appl. Meteor., 41, 558–572.

Hack JJ, Boville BA, Briegleb BP, Kiehl JT, Rasch PJ, Williamson DL (1993) Description of the NCAR Community Climate Model (CCM2). Technical Report NCAR/TN-382+STR, National Center for Atmospheric Research, 120 pp.

Hirota N, Takayabu YN, Watanabe M, Kimoto M (2011) Precipitation reproducibility over tropical oceans and its relationship to the double ITCZ problem in CMIP3 and MIROC5 climate models. J. Climate, 24, 4859-4873.

Holton JR, Wallace JM, Young JA (1971) On boundary layer dynamics and the ITCZ. J. Atmos. Sci., 28, 275-280.

Hourdin F, Grandpeix JY, Rio C, Bony S, Jam A, Cheruy F, Rochetin N, Fairhead L, Idelkadi A, Musat I, Dufresne JL, Lefebvre MP, Lahellec A, Roehrig R (2013) From LMDZ5A to LMDZ5B: revisiting the parameterizations of clouds and convection in the atmosperic component of the IPSL-CM5 climate model. Clim Dyn. doi:10.1007/s00382-012-1343-y

Huffman GJ, Robert F. Adler RF, Arkin P, Chang A, Ferraro R, Gruber A, Janowiak J, McNab A, Rudolf B, Udo Schneider U (1997) The Global Precipitation Climatology Project

(GPCP) Combined Precipitation Dataset. Bull. Amer. Meteor. Soc., 78, 5–20. doi: http://dx.doi.org/10.1175/1520-0477(1997)078<0005:TGPCPG>2.0.CO;2

Huffman GJ, Adler RF, Bolvin DT, Gu G, Nelkin EJ, Bowman KP, E.F. Stocker EF, Wolff DB (2007) The TRMM Multi-satellite Precipitation Analysis: Quasi-Global, Multi-Year, Combined-Sensor Precipitation Estimates at Fine Scale. J. Hydrometeor., 8, 33-55.

Huffman GJ, Bolvin DT (2011) Real-Time TRMM Multi-Satellite Precipitation Analysis Data Set Documentation. NASA/GSFC Laboratory for Atmospheres, 43 pp. ftp://meso.gsfc.nasa.gov/pub/trmmdocs/rt/3B4XRT_doc.pdf.

Huffman GJ, Bolvin DT (2012) GPCP Version 2.2 SG Combined Precipitation Data Set Documentation. ftp://precip.gsfc.nasa.gov/pub/gpcp-v2.2/doc/V2.2_doc.pdf, 46 pp.

Iversen T, Bentsen M, Bethke I, Debernard JB, Kirkevag A, Seland Ø, Drange H, Kristjansson JE, Medhaug I, Sand M, Seierstad IA (2013) The Norwegian Earth System Model, NorESM1-M – Part 2: Climate response and scenario projections. Geosci. Model Dev., 6, 389–415, doi:10.5194/gmd-6-389-2013, 2013.

Jiang et al (2012) Evaluation of cloud and water vapor simulations in CMIP5 climate models using NASA ‘A-Train’ satellite observations. J Geophys Res 117:D14105. doi:10.1029/ 2011JD017237

Kendon EJ, Roberts NM, Fowler HJ, Roberts MJ, Chan SC, Senior CA (2014) Heavier summer downpours with climate change revealed by weather forecast resolution model. Nature Climate Change 4:570-576. doi: 10.1038/nclimate2258

Klein SA, Zhang Y, Zelinka MD, Pincus R, Boyle J, Gleckler PJ (2013) Are climate model simulations of clouds improving? An evaluation using the ISCCP simulator. J Geophys Res Atmos 118:1329–1342. doi:10.1002/jgrd.50141

Lauer A, Hamilton K (2012) Simulating clouds with global climate models: a comparison on CMIP5 results with CMIP3 and satellite data. J Clim. doi:10.1175/JCLI-D-12-00451.1

Li G, Xie SP (2012) Origins of tropical-wide SST biases in CMIP multi-model ensembles. Geophys. Res. Lett., 39, L22703, doi:10.1029/2012GL053777.

Li G, Xie SP (2014) Tropical biases in CMIP5 multimodel ensemble: The excessive equatorial Pacific cold tongue and double ITCZ problems. J. Climate, 27, 1765-1780.

Lin J-L (2007) The double-ITCZ problem in IPCC AR4 Coupled GCMs: Oceanatmosphere feedback analysis. J. Clim., 20, 4497–4525.

Lohmann U, Roeckner E (1996) Design and performance of a new cloud microphysics scheme developed for the ECHAM general circulation model. Clim. Dyn., 557-572.

Misra V, Marx L, Brunke M, Zeng X (2008) The equatorial Pacific cold tongue bias in a coupled climate model, J. Climate, 21, 5852-5869.

Mizuta R, Yoshimura H, Murakami H, Matsueda M, Endo H, Ose T, Kamiguchi K, Hosaka M, Sugi M, Yukimoto S, Kusunoki S, Kitoh A (2012) Climate simulations using MRI-AGCM3.2 with 20-km grid. J. Meteor. Soc. Japan, 90A, 235-260, doi:10.2151/jmsj.2012-A12.

Murakami H, Wang Y, Yoshimura H, Mizuta R, Sugi M, Shindo E, Adachi Y, Yukimoto S, Hosaka M, Kusunoki S, Ose T, Kitoh A (2012) Future Changes in Tropical Cyclone Activity Projected by the New High-Resolution MRI-AGCM. J. Climate, 25, 3237-3260, doi:10.1175/JCLI-D-11-00415.1.

Neale RB, Richter JH, Conley AJ, Park S, Lauritzen PH, Gettelman A, Williamson DL, Rasch PJ, Vavrus SJ, Taylor MA, Collins WD, Zhang M, Lin SJ (2010) Description of the NCAR Community Atmosphere Model (CAM 4.0), Tech. Rep. NCAR/TN-485+STR, National Center for Atmospheric Research, Boulder, Colorado, USA.

Nicholson SE, Some B, McCollum J, Nelkin E, Klotter D, Berte Y, Diallo BM, Gaye I, Kpabeba G, Ndiaye O, Noukpozounkou JN, Tanu MM, Thiam A, Toure AA, Traore AK (2003) Validation of TRMM and Other Rainfall Estimates with a High-Density Gauge Dataset for West Africa. Part II: Validation of TRMM Rainfall Products. J. Appl. Meteor., 42, 1355–1368.

Pincus R, Batstone CP, Hofmann RJP, Taylor KE, Glecker PJ (2008) Evaluating the present-day simulation of clouds, precipitation, and radiation in climate models. J. Geophys. Res. Atmos., 113, D14209.

Rasch PJ, Kristj′ansson JE (1998) A comparison of the CCM3 model climate using diagnosed and predicted condensate parameterizations. J. Climate, 11, 1587—1614.

Rotstayn LD (1997) A physically based scheme for the treatment of stratiform clouds and precipitation in large-scale models. I: Description and evaluation of the microphysical processes. Q. J. R. Meteorol. Soc., 123, 1227-1282.

Rotstayn LD, Ryan BF, Katzfey JJ (2000) A scheme for calculation of the liquid fraction in mixed-phase stratiform clouds in large-scale models. Mon. Weather Rev., 128, 1070-1088.

Rotstayn LD, Jeffrey SJ, Collier MA, Dravitzki SM, Hirst AC, Syktus JI, Wong KK (2012) Aerosol- and greenhouse gas-induced changes in summer rainfall and circulation in the Australasian region: A study using single-forcing climate simulations. Atmos. Chem. Phys., 12, 6377-6404, doi:10.5194/acp-12-6377-2012.

von Salzen K, McFarlane NA (2002) Parameterization of the bulk effects of lateral and cloud-top entrainment in transient shallow cumulus clouds. J. Atmos. Sci., 1405-1429.

von Salzen K, Scinocca JF, McFarlane NA, Li J, Cole JNS, Plummer D, Verseghy D, Reader MC, Ma X, Lazare M, Solheim L (2013) The Canadian Fourth Generation Atmospheric Global Climate Model (CanAM4). Part I: Representation of Physical Processes. Atmosphere-Ocean. 51, 104-125.

Scinocca JF, McFarlane NA (2004) The Variability of Modeled Tropical Precipitation. J. Atmos. Sci., 61, 1993-2015.

Stanfield RE, Dong X, Xi B, Kennedy A, Del Genio AD, Minnis P, Jiang JH (2014) Assessment of NASA GISS CMIP5 and post-CMIP5 simulated clouds and TOA radiation budgets using satellite observations: Part I: Cloud fraction and properties. J. Climate, 27, no. 11, 4189-4208, doi:10.1175/JCLI-D-13-00558.1.

Stanfield RE, Dong X, Xi B, Del Genio AD, Minnis P, Doelling D, Loeb N (2015) Assessment of NASA GISS CMIP5 and Post-CMIP5 simulated clouds and TOA radiation budgets using satellite observations. Part II: TOA radiation budget and CREs. J. Climate, 28, no. 5, 1842-1864, doi:10.1175/JCLI-D-14-00249.1.

Stenz R, Dong X, Xi B, Kuligowski RJ (2014) Assessment of SCaMPR and NEXRAD Q2 Precipitation Estimates Using Oklahoma Mesonet Observations. J. Hydrometeor, 15, 2484–2500.

Stenz R, Dong X, Xi B, Feng Z, Kuligowski R (2015) Improving Satellite Quantitative Precipitation Estimates Using GOES-Retrieved Cloud Optical Depath. Accepted by J. Hydrometeorology.

Taylor KE (2001) Summarizing multiple aspects of model performance in a single diagram. J. Geophys. Res., 106 (D7), 7183–7192.

Taylor KE, Balaji V, Hankin S, Juckes M, Lawrence B (2010) CMIP5 Data Reference Syntax (DRS) and controlled vocabularies, 13 pp.

Taylor KE, Ronald J. Stouffer, Gerald A. Meehl (2012) An Overview of CMIP5 and the Experiment Design. Bull. Amer. Meteor. Soc., 93, 485–498.

Tiedtke M (1993) Representation of clouds in large-scale models. Mon. Wea. Rev., 121, 3040–3061.

Wang H, Su W (2013) Evaluating and understanding top of the atmosphere cloud radiative effects in International Panel on Climate Change (IPCC) AR5 CMIP5 models using satellite observations. J Geophys Res 118:683–699. doi:10.1029/2012JD018619.

Wilcox EM, Donner LJ (2007) The frequency of extreme rain events in satellite rain-rate estimates and an atmospheric general circulation model. J. Climate, 20, 53-69.

Wu T (2012) A Mass-Flux Cumulus Parameterization Scheme for Large-scale Models: Description and Test with Observations. Clim. Dyn., 38:725–744.

Yoshimura H, Mizuta R, Murakami H (2014) A spectral cumulus parameterization scheme interpolating between two convective updrafts with semi-Lagrangian calculation of transport by compensatory subsidence. Mon. Weather Rev., doi:10.1175/MWR-D-14-00068.1.

Yukimoto S, Yoshimura H, Hosaka M, Sakami T, Tsujino H, Hirabara M, Tanaka TY, Deushi M, Obata A, Nakano H, Adachi Y, Shindo E, Yabu S, Ose T, Kitoh A (2011) Meteorological Research Institute-Earth System Model Version 1 (MRI-ESM1) — Model Description —. Technical Reports of the Meteorological Research Institute, 64, 1-96. http://www.mri-jma.go.jp/Publish/Technical/index_jp.html

Yukimoto S, Adachi Y, Hosaka M, Sakami T, Yoshimura H, Hirabara M, Tanaka TY, Shindo E, Tsujino H, Deushi M, Mizuta R, Yabu S, Obata A, Nakano H, Koshiro T, Ose T, Kitoh A (2012) A New Global Climate Model of the Meteorological Research Institute: MRI-CGCM3 —Model Description and Basic Performance —. J. Meterol. Soc. Japan, 90A, 23-64, doi:10.2151/jmsj.2012-A02.

Zhang GJ, McFarlane NA (1995) Sensitivity of Climate Simulations to the Parameterization of Cumulus Convection in the Canadian Climate Centre General Circulation Model. Atmosphere-Ocean. 33, 407-446.

Zhang M, Lin W, Bretherton CS, Hack JJ, Rasch PJ (2003) A modified formulation of fractional stratiform condensation rate in the NCAR community atmospheric model CAM2. J. Geophys. Res., 108 (D1).

Zhao M, Held IM, Lin SJ, Vecchi GA (2009) Simulations of global hurricane climatology, interannual variability, and response to global warming using a 50km resolution GCM. J. Climate, 22, 6653-6678.

Figure Captions

Fig. 1 – Comparisons of area-weighted mean precipitation (a) annually, in (b) January, and in (C) July between GPCP (black) and TRMM (red) observations and 29 GCM simulations used in this study over Tropical and sub-tropical regions (±40° latitude). The black/red lines each represent the mean of GPCP/TRMM observations, respectively, while the blue line represents the GCM ensemble mean. All results are calculated over the full study period, January 2000 to December 2005.

Fig. 2 – Annually averaged regional mean precipitation over ±40° latitudes from (a) GPCP and (b) TRMM observations and (c) the GCM Ensemble mean during the 6-yr study period. The annual area-weighted means for each dataset are shown on the upper right corner of the image. The green box in each image represents the Area Of Focus (AOF): 2° S to 21° N and 180° W to 110° W, defined in this study.

Fig. 3 – Seasonal precipitation in the Pacific ITCZ from GPCP and TRMM observations. The green box in each image represents the AOF (2° S to 21° N and 180° W to 110° W) defined in this study. The regional mean represents the average amount of seasonal precipitation within the AOF for the respective month during the 6-yr study period.

Fig. 4 – A visual example defining Intertropical Convergence Zone (ITCZ) boundaries within the AOF using monthly data from the Australian Access 1-3 in January. The green box is the AOF defined in this study, the orange lines represent the upper and lower boundaries of the ITCZ using the method described, and the white line represents the derived centerline based on upper and lower boundaries. White, green, and red dots indicate a gridded precipitation rate greater than 4, 5, and 6 millimeters per day, respectively.

Fig. 5 – Three idealized examples of potential biases found when comparing GCM simulated (blue, red, or green) and observed (black) precipitation in the ITCZ: (a) location bias shown by a shift northward in the simulated ITCZ, (b) magnitude bias shown as an intensification of precipitation in the simulated ITCZ, and (c) width bias shown as a broadening of the simulated ITCZ, when compared to the observed ITCZ.

Fig. 6 – Position of the ITCZ centerline as derived by our algorithm, shown as each respective GCM minus observations. Each month is color coded as shown in the legend. The horizontal black line found near the center of the diagram can be interepreted as the centerline derived from GPCP and TRMM observations. As such, if the colored bar is above (below) the black line, this suggests the centerline of the ITCZ simulated by a GCM is located more northward (southward) compared to observations. Each bar is vertically stacked for each respective GCM, meaning the bias found in each month should be measured as the length of respectively colored bar and not as the distance from the black line. Bars are stacked with January closest to the black bar, and expands outward, stacked vertically, progressing by month to December.

Fig. 7 – As in Fig. 6, except showing the width of the ITCZ as derived by our algorithm, calculated as the distance between the upper and lower boundaries of the ITCZ (orange lines the

in Fig. 4), shown as each respective GCM minus (a) GPCP or (b) TRMM observations. The colored bars above (below) the horizontal black line represent months where the vertical width of the simulated ITCZ of the respective GCM was found to wider (thinner) than the observed ITCZ.

Fig. 8 – As in Fig. 6, except showing the magnitude of precipitation within the ITCZ as derived by our algorithm, shown as each respective GCM minus (a) GPCP or (b) TRMM observations. The colored bars above (below) the horizontal black line represent months where the of precipitation of the respective GCM was found to simulated stronger (weaker) than that of the respective observations.

Fig. 9 - As in Fig. 6, except showing the ITCZ precipitation comparison between AMIP and historical ocean-coupled (CMIP) precipitation given as CMIP minus AMIP. The colored bars above (below) the horizontal black line represent months where precipitation in the respective GCM is found to be greater in the CMIP (AMIP) simulation.

Fig. 10 - Algorithm results using averaged monthly precipitation from the BCC-CSM1-1 GCM.

Table Captions

Table 1 – Summary of the 29 GCMs used in this study, along with their spatial resolution (longitude × latitude). Models across from each other (horizonatally) are considered to be linked when comparing historical and AMIP simulated precipitation in section 4c of this study

Table 2 – A brief summary of the convective and stratiform precipitation parameterizations from selected CMIP5 GCMs

Supplemental Figure Captions

Supplemental Fig. A – Table version of Fig. 6 provided with quantitative values. Values in each cell depict the average monthly value of centerline shift (degrees of latitude) between each respective GCM and the averaged location from GPCP and TRMM observations, given as the model minus the observations. Cells are shaded blue (red) in increasing intensity when the centerline of the GCM was found to be more northward (southward) compared to the observations. The color of the text used within the cells is irrelevant within these supplemental figures and is only varied to provide easier reading and more contrast in available colors.

Supplemental Fig. B – Table version of Fig. 7a provided with quantitative values. Values in each cell depict the difference in average monthly ITCZ width (degrees of latitude) between each respective GCM and GPCP observations, given as the model minus observations. Cells are shaded red (blue) in increasing intensity when the width of the ITCZ simulated by the GCM was found to be wider (thinner) compared to the GPCP ITCZ width.

Supplemental Fig. C – Same as Fig. B but using TRMM observational results (Fig. 7b).

Supplemental Fig. D – Table version of Figure 8a provided with quantitative values. Values in each cell depict the difference in precipitation (mm/day) between each GCM simulation and GPCP observation when averaged within ±4° latitude of the observed centerline, given as the model minus observations. Cells are shaded red (blue) in increasing intensity when the magnitude of precipitation in the GCM was found to be stronger (weaker) compared to the magnitude of precipitation within the GPCP ITCZ.

Supplemental Fig. E – Same as Fig. D but using TRMM observational results (Fig. 8b).

Supplemental Fig. F - Table version of Fig. 9 provided with quantitative values. Values in each cell depict the differences in precipitation (mm/day) between CMIP and AMIP simulations when averaged within ±4° latitude of the observed centerline, given as CMIP minus AMIP. Cells are shaded red (blue) in increasing intensity when the magnitude of precipitation in the CMIP version of the GCM was found to be stronger (weaker) compared to its AMIP counterpart.

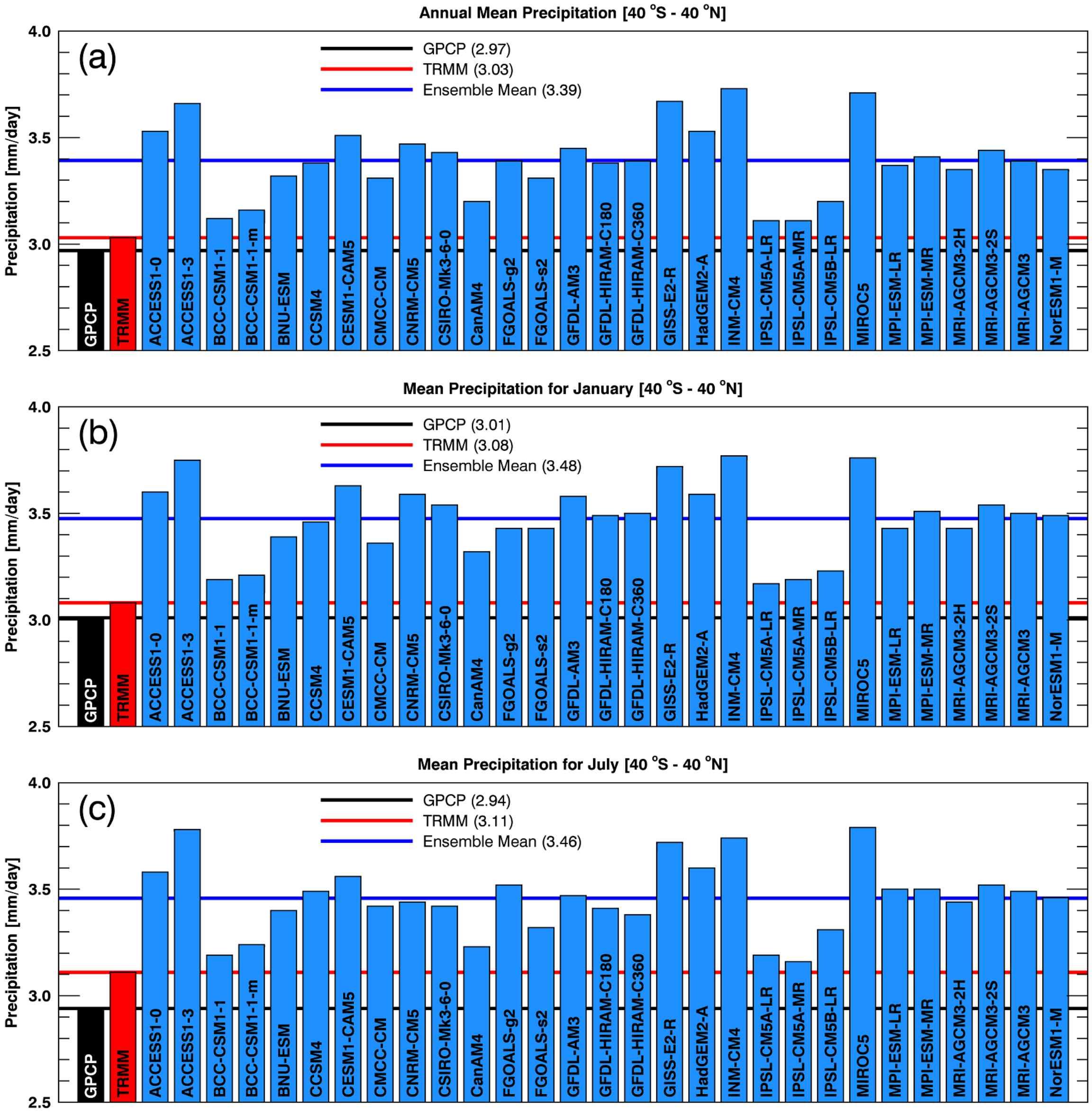

Fig. 1 – Comparisons of area-weighted mean precipitation (a) annually, in (b) January, and in (C) July between GPCP (black) and TRMM (red) observations and 29 GCM simulations used in this study over Tropical and sub-tropical regions (±40° latitude). The black/red lines each represent the mean of GPCP/TRMM observations, respectively, while the blue line represents the GCM ensemble mean. All results are calculated over the full study period, January 2000 to December 2005.

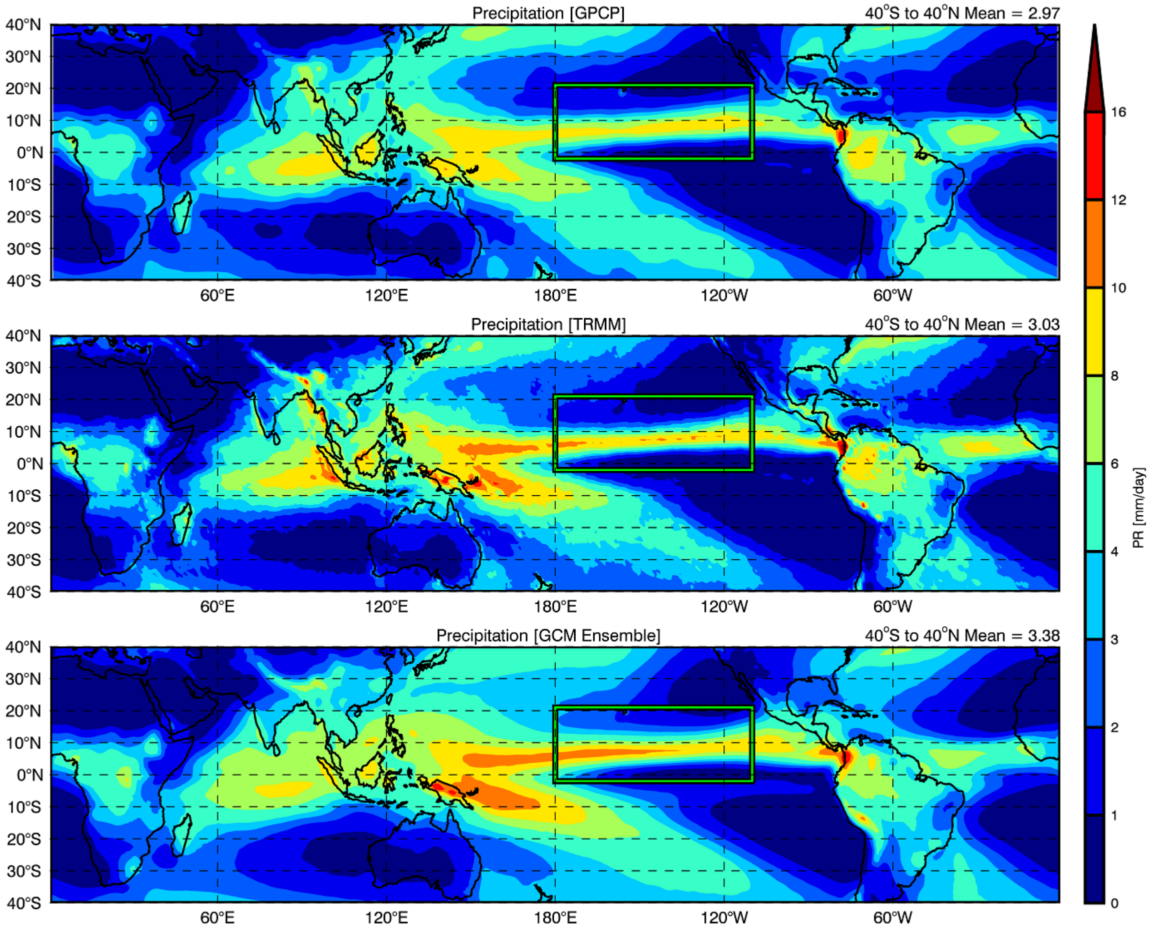

Fig. 2 – Annually averaged regional mean precipitation over ±40° latitudes from (a) GPCP and (b) TRMM observations and (c) the GCM Ensemble mean during the 6-yr study period. The annual area-weighted means for each dataset are shown on the upper right corner of the image. The green box in each image represents the Area Of Focus (AOF): 2° S to 21° N and 180° W to 110° W, defined in this study.

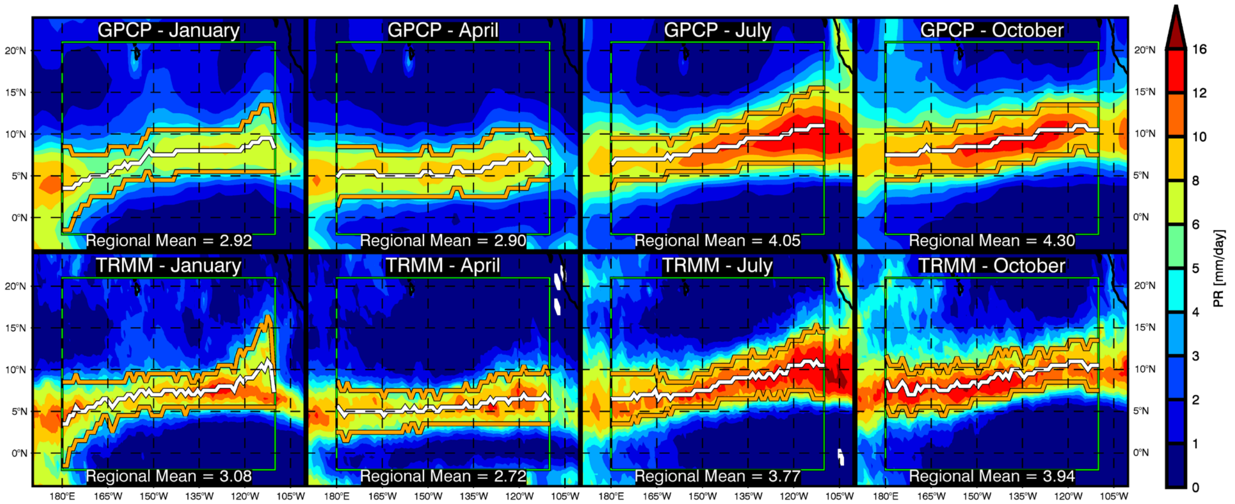

Fig. 3 – Seasonal precipitation in the Pacific ITCZ from GPCP and TRMM observations. The green box in each image represents the AOF (2° S to 21° N and 180° W to 110° W) defined in this study. The regional mean represents the average amount of seasonal precipitation within the AOF for the respective month during the 6-yr study period.

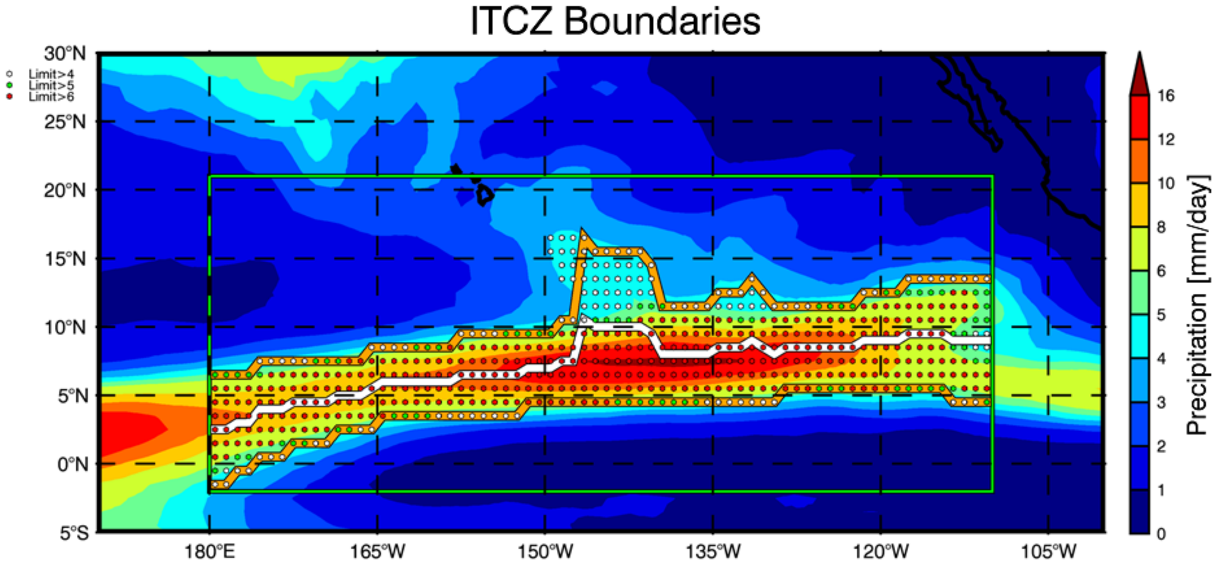

Fig. 4 – A visual example defining Intertropical Convergence Zone (ITCZ) boundaries within the AOF using monthly data from the Australian Access 1-3 in January. The green box is the AOF defined in this study, the orange lines represent the upper and lower boundaries of the ITCZ using the method described, and the white line represents the derived centerline based on upper and lower boundaries. White, green, and red dots indicate a gridded precipitation rate greater than 4, 5, and 6 millimeters per day, respectively.

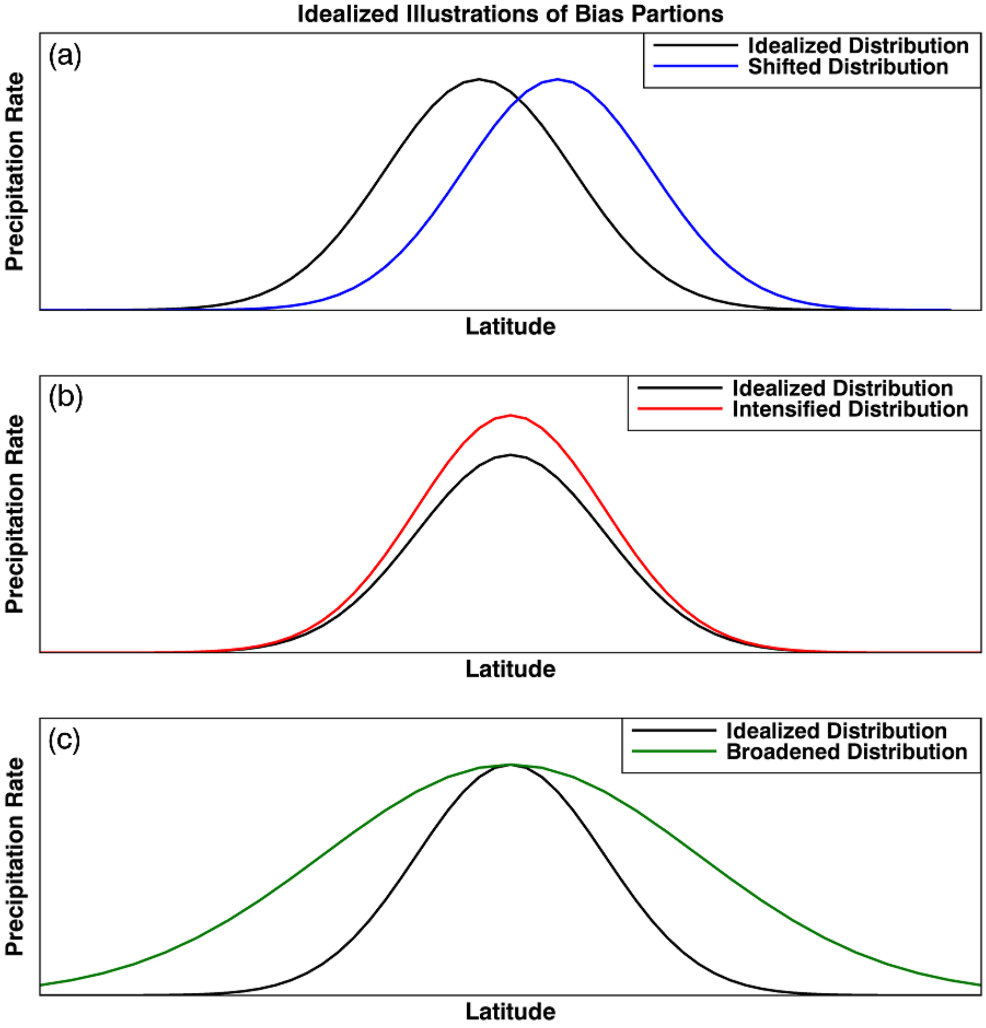

Fig. 5 – Three idealized examples of potential biases found when comparing GCM simulated (blue, red, or green) and observed (black) precipitation in the ITCZ: (a) location bias shown by a shift northward in the simulated ITCZ, (b) magnitude bias shown as an intensification of precipitation in the simulated ITCZ, and (c) width bias shown as a broadening of the simulated ITCZ, when compared to the observed ITCZ.

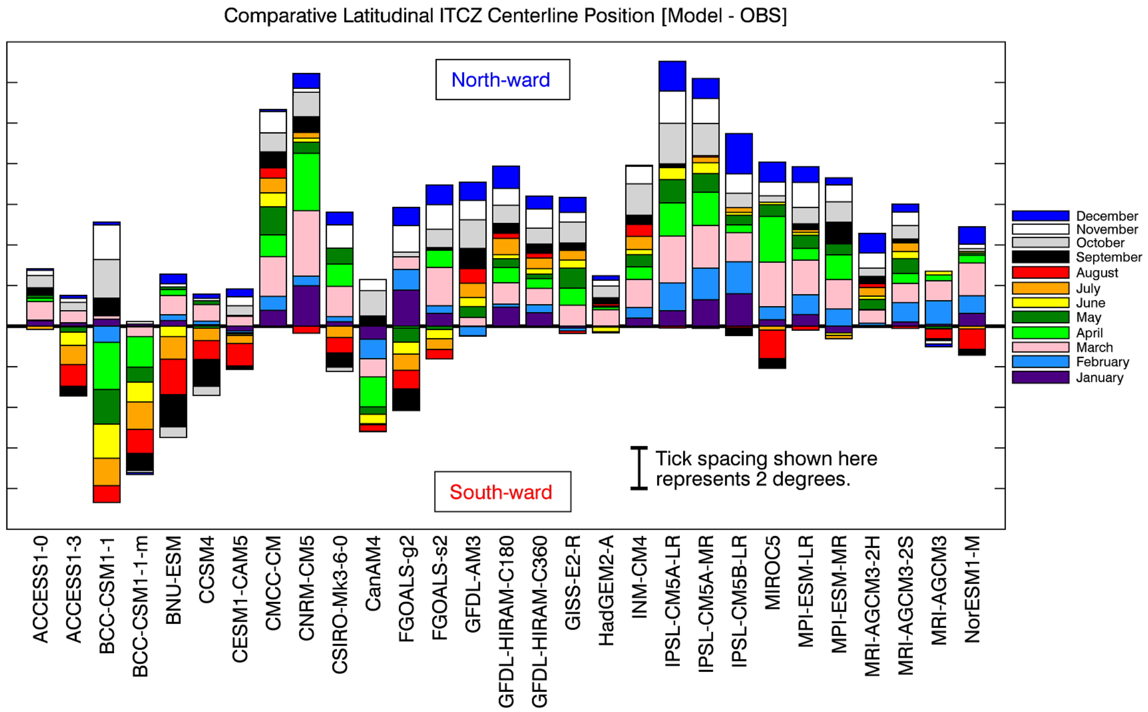

Fig. 6 – Position of the ITCZ centerline as derived by our algorithm, shown as each respective GCM minus observations. Each month is color coded as shown in the legend. The horizontal black line found near the center of the diagram can be interpreted as the centerline derived from GPCP and TRMM observations. As such, if the colored bar is above (below) the black line, this suggests the centerline of the ITCZ simulated by a GCM is located more northward (southward) compared to observations. Each bar is vertically stacked for each respective GCM, meaning the bias found in each month should be measured as the length of respectively colored bar and not as the distance from the black line. Bars are stacked with January closest to the black bar, and expands outward, stacked vertically, progressing by month to December.

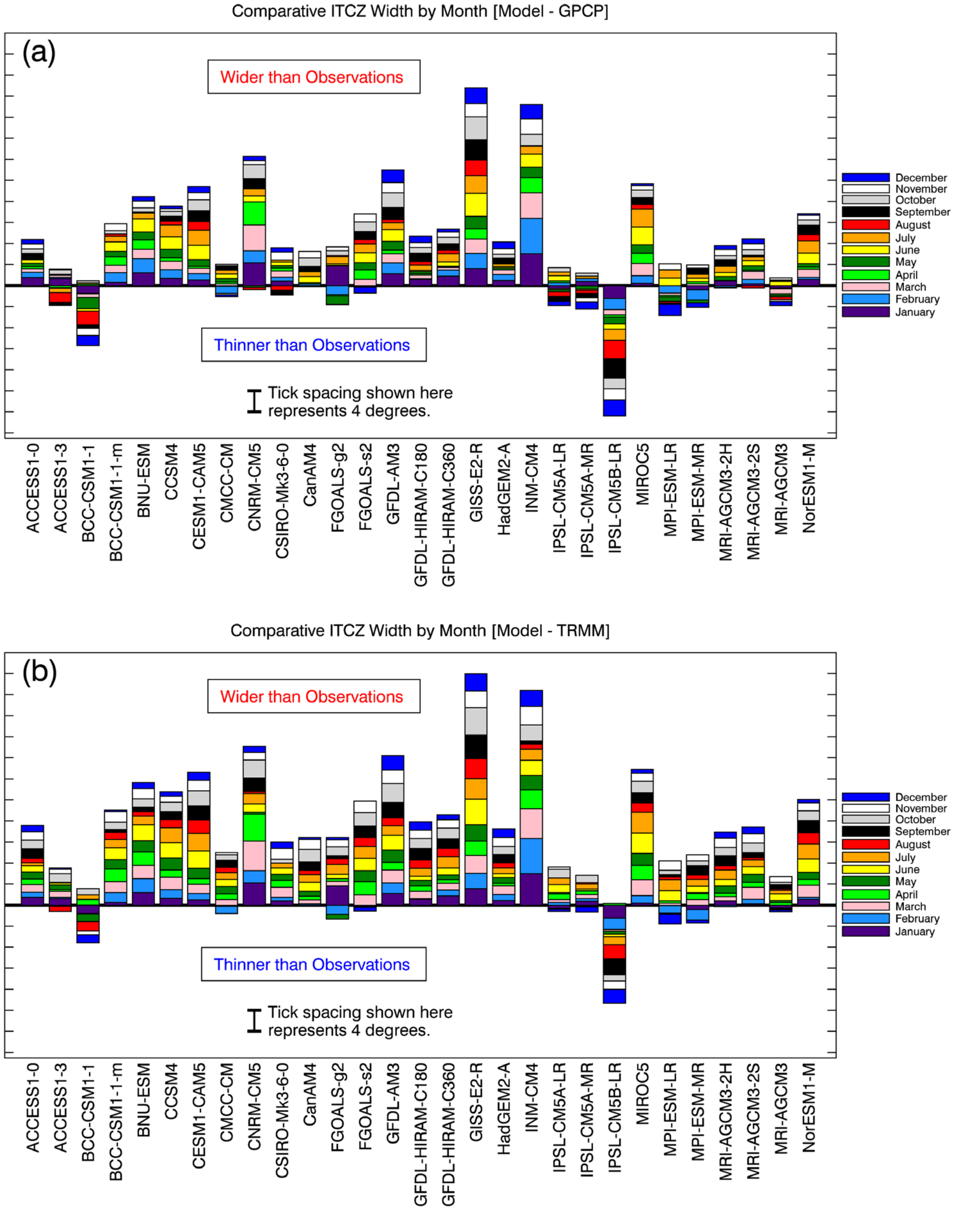

Fig. 7 – As in Fig. 6, except showing the width of the ITCZ as derived by our algorithm, calculated as the distance between the upper and lower boundaries of the ITCZ (orange lines the in Fig. 4), shown as each respective GCM minus (a) GPCP or (b) TRMM observations. The colored bars above (below) the horizontal black line represent months where the vertical width of the simulated ITCZ of the respective GCM was found to wider (thinner) than the observed ITCZ.

Comparative ITCZ Precipitation Magnitude [Model - GPCP]

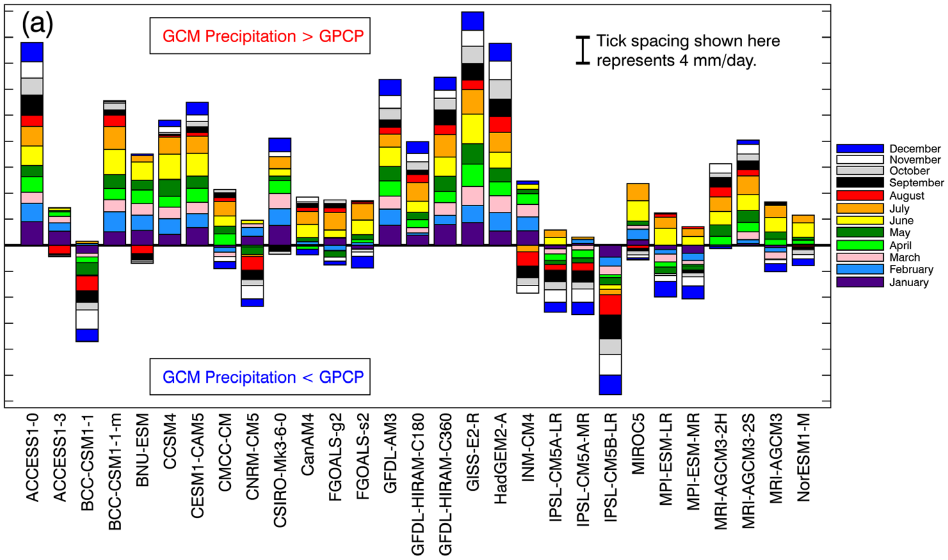

Comparative ITCZ Precipitation Magnitude [Model - TRMM]

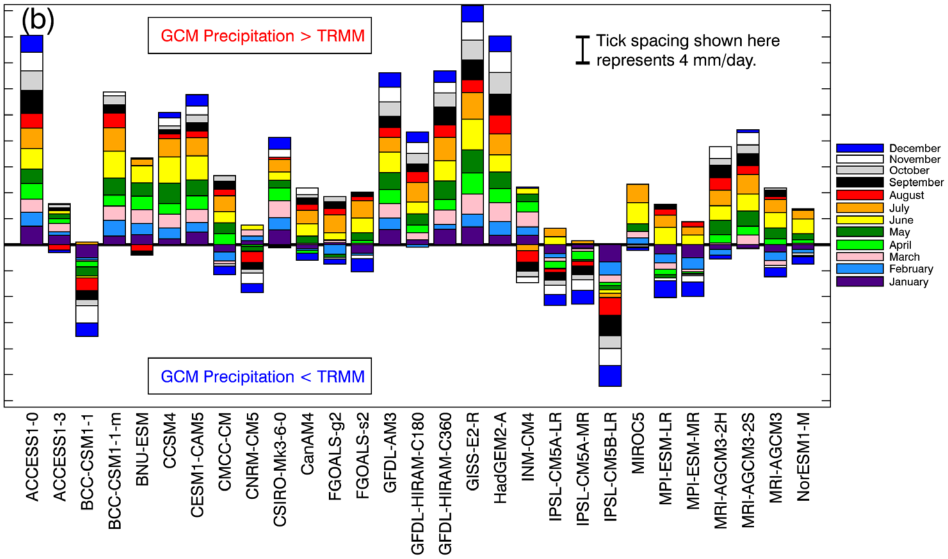

Fig. 8 – As in Fig. 6, except showing the magnitude of precipitation within the ITCZ as derived by our algorithm, shown as each respective GCM minus (a) GPCP or (b) TRMM observations. The colored bars above (below) the horizontal black line represent months where the of precipitation of the respective GCM was found to simulated stronger (weaker) than that of the respective observations.

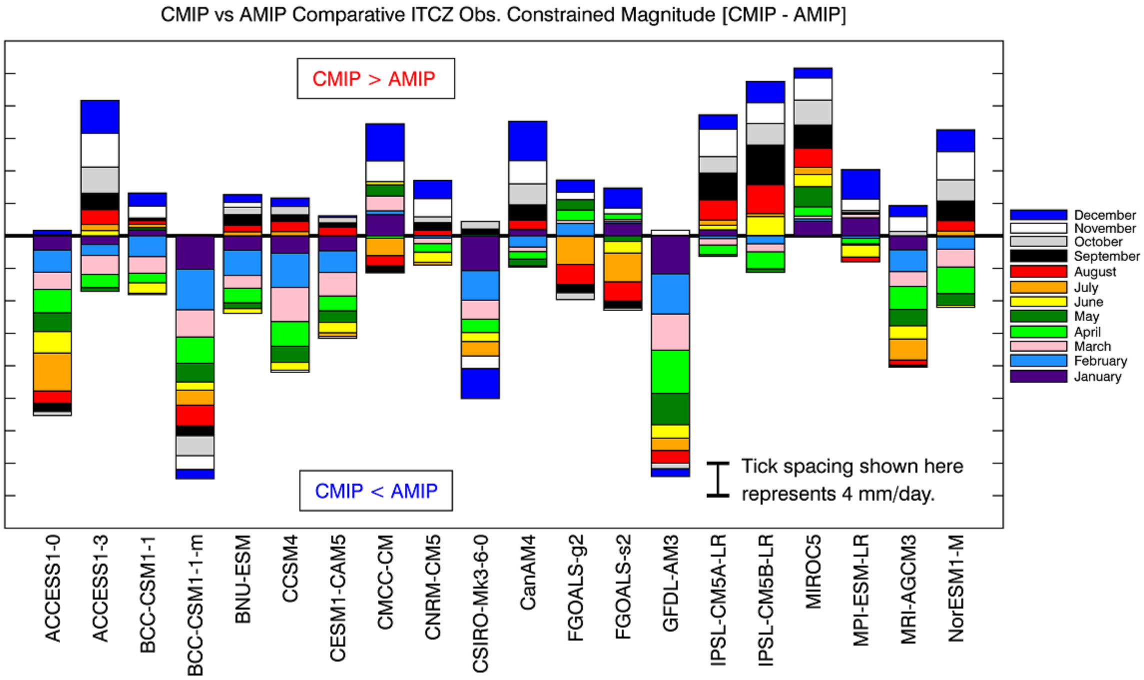

Fig. 9 - As in Fig. 6, except showing the ITCZ precipitation comparison between AMIP and historical ocean-coupled (CMIP) precipitation given as CMIP minus AMIP. The colored bars above (below) the horizontal black line represent months where precipitation in the respective GCM is found to be greater in the CMIP (AMIP) simulation.

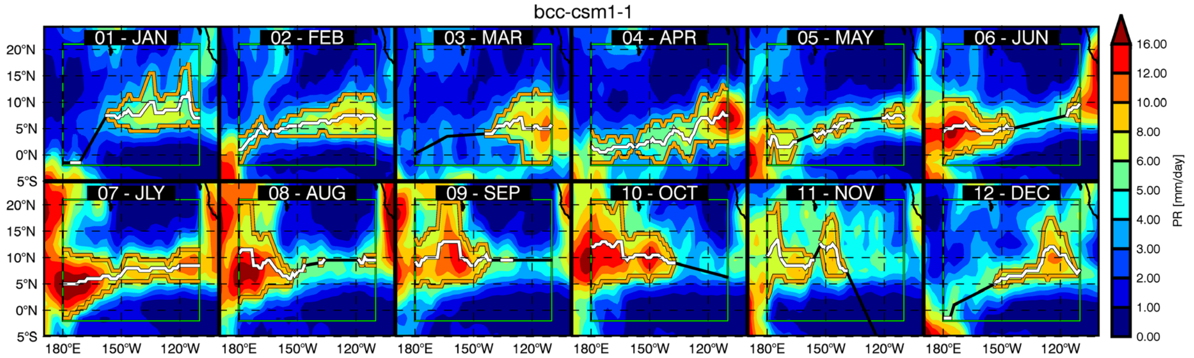

Fig. 10 - Algorithm results using averaged monthly precipitation from the BCC-CSM1-1 GCM, shown due to its chaotic pattern and undersimulaiton of precipitation when compared to GPCP and TRMM. As in Fig. 4, the green box is the AOF defined in this study, the orange lines represent the upper and lower boundaries of the ITCZ using the method described, and the white line represents the derived centerline based on upper and lower boundaries. The black line represents where the algorithm was forced to interpolate/extrapolate the centerline position due to precipitation values being below the threshold for that given latitudinal band.

Table 1 – Summary of the 29 GCMs used in this study, along with their spatial resolution (longitude × latitude). Models across from each other (horizontally) are considered to be linked when comparing historical and AMIP simulated precipitation in section 4c of this study.

#	AMIP Model	Resolution	Linked Historical Model
1	ACCESS 1-0	1.875 x 1.25	ACCESS1-0
2	ACCESS 1-3	1.875 x 1.25	ACCESS1-3
3	BCC-CSM1-1	2.8125 x 2.8125	BCC-CSM1-1
4	BCC-CSM1-1-m	1.25 x 1.25	BCC-CSM1-1-m
5	BNU-ESM	2.8125 x 2.8125	BNU-ESM
6	CCSM4	1.25 x 0.9375	CCSM4
7	CESM1-CAM5	1.25 x 0.9375	CESM1-CAM5
8	CMCC-CM	0.75 x 0.75	CMCC-CM
9	CNRM-CM5	1.4 x 1.4	CNRM-CM5
10	CSIRO-Mk3-6-0	1.875 x 1.875	CSIRO-Mk3-6-0
11	CanAM4	2.8125 x 2.8125	CanCM4
12	FGOALS-g2	2.815 x 3	FGOALS-g2
13	FGOALS-s2	2.815 x 1.666	FGOALS-g2
14	GFDL-AM3	2.5 x 2	GFDL-CM3
15	GFDL-HIRAM-C180	0.625 x 0.5	-
16	GFDL-HIRAM-C360	0.3125 x 0.25	-
17	GISS-E2-R	2.5 x 2	-
18	HadGEM2-A	1.875 x 1.25	-
19	INM-CM4	2 x 1.5	-
20	IPSL-CM5A-LR	3.75 x 1.875	IPSL-CM5A-LR
21	IPSL-CM5A-MR	2.5 x 1.25	-
22	IPSL-CM5B-LR	3.75 x 1.875	IPSL-CM5B-LR
23	MIROC5	1.4 x 1.4	MIROC5
24	MPI-ESM-LR	1.875 x 1.875	MPI-ESM-LR
25	MPI-ESM-MR	1.875 x 1.875	-
26	MRI-AGCM3-2H	0.5625 x 0.5625	-
27	MRI-AGCM3-2S	0.1875 x 0.1875	-
28	MRI-AGCM3	1.125 x 1.125	MRI-CGCM3
29	NorESM1-M	2.5 x 1.8947	NorESM1-M

Table 2 – A brief summary of the convective and stratiform precipitation parameterizations from selected CMIP5 GCMs

Model Name	Convective Precipitation	Stratiform Precipitation
BCC-CSM1-1 BCC-CSM1-1-m	Deep Convection (Wu, 2012) Shallow/middle Tropospheric convection (Hack et al., 1993)	Rasch and Kristjánsson (1998) Zhang et al. (2003)
CanAM4	Deep convection is parameterized based on the method of Zhang and McFarlane, 1995 with modifications to limit its application to cloud ensembles with top above the freezing level and to use a prognostic, CAPE based closure (Scinocca and McFarlane, 2004). Shallow convection is parameterized using the mass flux scheme of von Salzen and McFarlane, 2002 and is allowed to occur concurrently with deep convection.	Subgrid-scale stratiform clouds are parameterized using a statistical cloud scheme (Chaboureau and Bechtold, 2002). Microphysical processes are parameterized based on the approach of Lohmann and Roeckner, 1996 with improvements being applied to several processes (von Salzen, et al., 2013).
CSIRO-Mk3-6-0	Bulk mass-flux convection scheme with a simple stability-dependent closure (Gregory and Rowntree 1990) modified by the inclusion of downdrafts (Gregory and Allen 1991).	Bulk condensational scheme with prognostic variables for cloud liquid water and cloud ice (Rotstayn 1997, Rotstayn et al. 2000). Cloud droplet number concentration is empirically related to aerosol concentration for the first and second indirect effects (Rotstayn et al., 2012).
GFDL-AM3 GFDL-CM3	Deep cumulus is parameterized as an ensemble of updraft cells, along with mesoscale updrafts and downdrafts (Donner, 1993; Donner et al., 2001; Wilcox and Donner, 2007). Several modifications have been made in AM3 (Donner et al., 2011) for computational efficiency or simulation improvement. The relative numbers of updraft cells with varying entrainment are based on observations of the probability distribution function for vertical velocity in deep convection. The closure for the deep cumulus parameterization produces cumulus heating which relaxes convective available potential energy towards a threshold value. Shallow cumulus convection follows Bretherton et al. (2004), modified as in Zhao et al. (2009) and Donner et al. (2011). Shallow cumulus is parameterized as single, buoyancy-sorting plume, with a closure for cloud-base mass flux based on boundary-layer turbulence kinetic energy.	Stratiform clouds are parameterized following Tiedtke (1993), with modifications described in Donner et al. (2011). This parameterization consists of prognostic equations for cloud fraction, liquid, and ice, with sources and sinks due to advection, deep convection, and large-scale processes (e.g., condensation, deposition, radiative cooling, cloud erosion, and evaporation).
GFDL-HIRAM-C180 GFDL-HIRAM-C360	Bretherton et al. (2004) approach, with modifications discussed in Zhao et al. (2009).	Cloud fraction is determined diagnostically based on grid-box mean water content (Zhao et al., 2009), with single-moment microphysics as in Anderson et al. (2004).
MRI-AGCM3 MRI-CGCM3	Prognostic cloud water/ice mixing ratio and concentrations (MRI-TMBC) (Yukimoto et al, 2006)	Spectral mass flux scheme (Yoshimura et al. 2014)
MRI-AGCM3-2S MRI-AGCM-2H	Prognostic cloud water mixing ratio and cloud cover based on Tiedtke (1993)	Spectral mass flux scheme (Yoshimura et al. 2014)
NorESM1-M	Methods described in: Neale et al. (2010) Bentsen et al. (2013) Iversen et al. (2013)	

Supplemental Figures

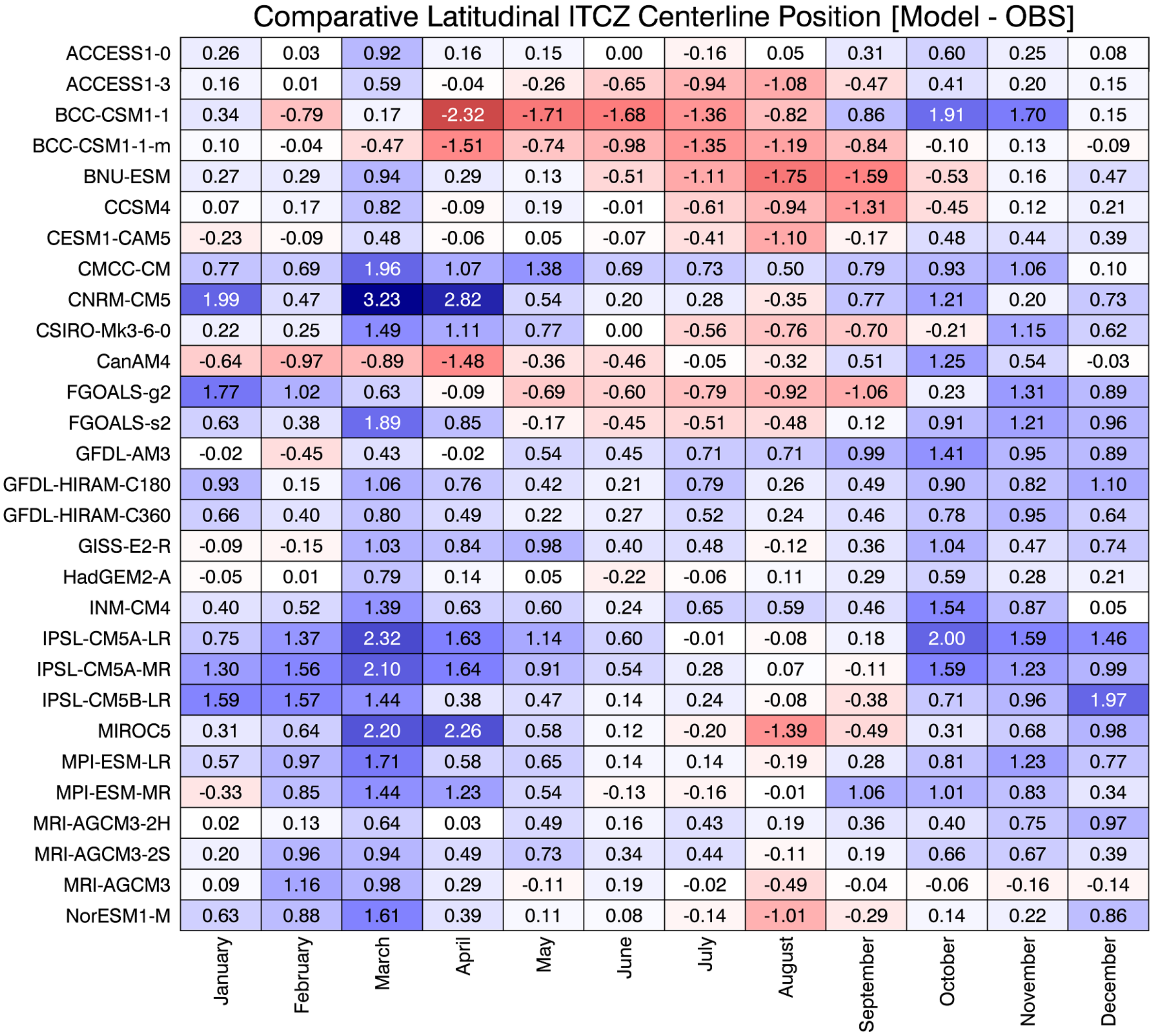

Comparative Latitudinal ITCZ Centerline Position [Model - OBS]

	January	February	March	April	May	June	July	August	September	October	November	December
ACCESS1-0	0.26	0.03	0.92	0.16	0.15	0.00	-0.16	0.05	0.31	0.60	0.25	0.08
ACCESS1-3	0.16	0.01	0.59	-0.04	-0.26	-0.65	-0.94	-1.08	-0.47	0.41	0.20	0.15
BCC-CSM1-1	0.34	-0.79	0.17	-2.32	-1.71	-1.68	-1.36	-0.82	0.86	1.91	1.70	0.15
BCC-CSM1-1-m	0.10	-0.04	-0.47	-1.51	-0.74	-0.98	-1.35	-1.19	-0.84	-0.10	0.13	-0.09
BNU-ESM	0.27	0.29	0.94	0.29	0.13	-0.51	-1.11	-1.75	-1.59	-0.53	0.16	0.47
CCSM4	0.07	0.17	0.82	-0.09	0.19	-0.01	-0.61	-0.94	-1.31	-0.45	0.12	0.21
CESM1-CAM5	-0.23	-0.09	0.48	-0.06	0.05	-0.07	-0.41	-1.10	-0.17	0.48	0.44	0.39
CMCC-CM	0.77	0.69	1.96	1.07	1.38	0.69	0.73	0.50	0.79	0.93	1.06	0.10
CNRM-CM5	1.99	0.47	3.23	2.82	0.54	0.20	0.28	-0.35	0.77	1.21	0.20	0.73
CSIRO-Mk3-6-0	0.22	0.25	1.49	1.11	0.77	0.00	-0.56	-0.76	-0.70	-0.21	1.15	0.62
CanAM4	-0.64	-0.97	-0.89	-1.48	-0.36	-0.46	-0.05	-0.32	0.51	1.25	0.54	-0.03
FGOALS-g2	1.77	1.02	0.63	-0.09	-0.69	-0.60	-0.79	-0.92	-1.06	0.23	1.31	0.89
FGOALS-s2	0.63	0.38	1.89	0.85	-0.17	-0.45	-0.51	-0.48	0.12	0.91	1.21	0.96
GFDL-AM3	-0.02	-0.45	0.43	-0.02	0.54	0.45	0.71	0.71	0.99	1.41	0.95	0.89
GFDL-HIRAM-C180	0.93	0.15	1.06	0.76	0.42	0.21	0.79	0.26	0.49	0.90	0.82	1.10
GFDL-HIRAM-C360	0.66	0.40	0.80	0.49	0.22	0.27	0.52	0.24	0.46	0.78	0.95	0.64
GISS-E2-R	-0.09	-0.15	1.03	0.84	0.98	0.40	0.48	-0.12	0.36	1.04	0.47	0.74
HadGEM2-A	-0.05	0.01	0.79	0.14	0.05	-0.22	-0.06	0.11	0.29	0.59	0.28	0.21
INM-CM4	0.40	0.52	1.39	0.63	0.60	0.24	0.65	0.59	0.46	1.54	0.87	0.05
IPSL-CM5A-LR	0.75	1.37	2.32	1.63	1.14	0.60	-0.01	-0.08	0.18	2.00	1.59	1.46
IPSL-CM5A-MR	1.30	1.56	2.10	1.64	0.91	0.54	0.28	0.07	-0.11	1.59	1.23	0.99
IPSL-CM5B-LR	1.59	1.57	1.44	0.38	0.47	0.14	0.24	-0.08	-0.38	0.71	0.96	1.97
MIROC5	0.31	0.64	2.20	2.26	0.58	0.12	-0.20	-1.39	-0.49	0.31	0.68	0.98
MPI-ESM-LR	0.57	0.97	1.71	0.58	0.65	0.14	0.14	-0.19	0.28	0.81	1.23	0.77
MPI-ESM-MR	-0.33	0.85	1.44	1.23	0.54	-0.13	-0.16	-0.01	1.06	1.01	0.83	0.34
MRI-AGCM3-2H	0.02	0.13	0.64	0.03	0.49	0.16	0.43	0.19	0.36	0.40	0.75	0.97
MRI-AGCM3-2S	0.20	0.96	0.94	0.49	0.73	0.34	0.44	-0.11	0.19	0.66	0.67	0.39
MRI-AGCM3	0.09	1.16	0.98	0.29	-0.11	0.19	-0.02	-0.49	-0.04	-0.06	-0.16	-0.14
NorESM1-M	0.63	0.88	1.61	0.39	0.11	0.08	-0.14	-1.01	-0.29	0.14	0.22	0.86

Supplemental Fig. A – Table version of Fig. 6 provided with quantitative values. Values in each cell depict the average monthly value of centerline shift (degrees of latitude) between each respective GCM and the averaged location from GPCP and TRMM observations, given as the model minus the observations. Cells are shaded blue (red) in increasing intensity when the centerline of the GCM was found to be more northward (southward) compared to the observations. The color of the text used within the cells is irrelevant within these supplemental figures and is only varied to provide easier reading and more contrast in available colors.

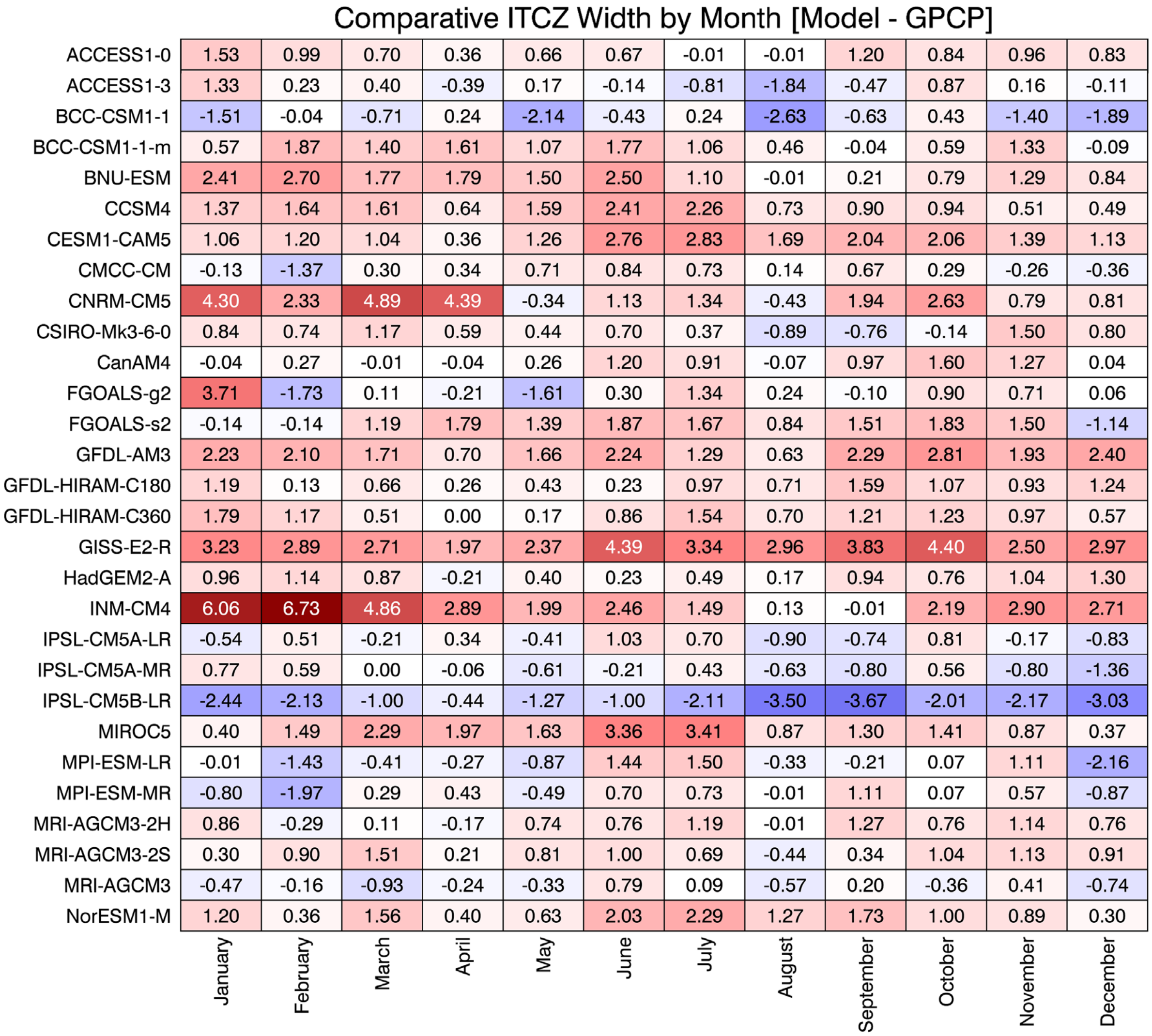

Comparative ITCZ Width by Month [Model - GPCP]

	January	February	March	April	May	June	July	August	September	October	November	December
ACCESS1-0	1.53	0.99	0.70	0.36	0.66	0.67	-0.01	-0.01	1.20	0.84	0.96	0.83
ACCESS1-3	1.33	0.23	0.40	-0.39	0.17	-0.14	-0.81	-1.84	-0.47	0.87	0.16	-0.11
BCC-CSM1-1	-1.51	-0.04	-0.71	0.24	-2.14	-0.43	0.24	-2.63	-0.63	0.43	-1.40	-1.89
BCC-CSM1-1-m	0.57	1.87	1.40	1.61	1.07	1.77	1.06	0.46	-0.04	0.59	1.33	-0.09
BNU-ESM	2.41	2.70	1.77	1.79	1.50	2.50	1.10	-0.01	0.21	0.79	1.29	0.84
CCSM4	1.37	1.64	1.61	0.64	1.59	2.41	2.26	0.73	0.90	0.94	0.51	0.49
CESM1-CAM5	1.06	1.20	1.04	0.36	1.26	2.76	2.83	1.69	2.04	2.06	1.39	1.13
CMCC-CM	-0.13	-1.37	0.30	0.34	0.71	0.84	0.73	0.14	0.67	0.29	-0.26	-0.36
CNRM-CM5	4.30	2.33	4.89	4.39	-0.34	1.13	1.34	-0.43	1.94	2.63	0.79	0.81
CSIRO-Mk3-6-0	0.84	0.74	1.17	0.59	0.44	0.70	0.37	-0.89	-0.76	-0.14	1.50	0.80
CanAM4	-0.04	0.27	-0.01	-0.04	0.26	1.20	0.91	-0.07	0.97	1.60	1.27	0.04
FGOALS-g2	3.71	-1.73	0.11	-0.21	-1.61	0.30	1.34	0.24	-0.10	0.90	0.71	0.06
FGOALS-s2	-0.14	-0.14	1.19	1.79	1.39	1.87	1.67	0.84	1.51	1.83	1.50	-1.14
GFDL-AM3	2.23	2.10	1.71	0.70	1.66	2.24	1.29	0.63	2.29	2.81	1.93	2.40
GFDL-HIRAM-C180	1.19	0.13	0.66	0.26	0.43	0.23	0.97	0.71	1.59	1.07	0.93	1.24
GFDL-HIRAM-C360	1.79	1.17	0.51	0.00	0.17	0.86	1.54	0.70	1.21	1.23	0.97	0.57
GISS-E2-R	3.23	2.89	2.71	1.97	2.37	4.39	3.34	2.96	3.83	4.40	2.50	2.97
HadGEM2-A	0.96	1.14	0.87	-0.21	0.40	0.23	0.49	0.17	0.94	0.76	1.04	1.30
INM-CM4	6.06	6.73	4.86	2.89	1.99	2.46	1.49	0.13	-0.01	2.19	2.90	2.71
IPSL-CM5A-LR	-0.54	0.51	-0.21	0.34	-0.41	1.03	0.70	-0.90	-0.74	0.81	-0.17	-0.83
IPSL-CM5A-MR	0.77	0.59	0.00	-0.06	-0.61	-0.21	0.43	-0.63	-0.80	0.56	-0.80	-1.36
IPSL-CM5B-LR	-2.44	-2.13	-1.00	-0.44	-1.27	-1.00	-2.11	-3.50	-3.67	-2.01	-2.17	-3.03
MIROC5	0.40	1.49	2.29	1.97	1.63	3.36	3.41	0.87	1.30	1.41	0.87	0.37
MPI-ESM-LR	-0.01	-1.43	-0.41	-0.27	-0.87	1.44	1.50	-0.33	-0.21	0.07	1.11	-2.16
MPI-ESM-MR	-0.80	-1.97	0.29	0.43	-0.49	0.70	0.73	-0.01	1.11	0.07	0.57	-0.87
MRI-AGCM3-2H	0.86	-0.29	0.11	-0.17	0.74	0.76	1.19	-0.01	1.27	0.76	1.14	0.76
MRI-AGCM3-2S	0.30	0.90	1.51	0.21	0.81	1.00	0.69	-0.44	0.34	1.04	1.13	0.91
MRI-AGCM3	-0.47	-0.16	-0.93	-0.24	-0.33	0.79	0.09	-0.57	0.20	-0.36	0.41	-0.74
NorESM1-M	1.20	0.36	1.56	0.40	0.63	2.03	2.29	1.27	1.73	1.00	0.89	0.30

Supplemental Fig. B – Table version of Fig. 7a provided with quantitative values. Values in each cell depict the difference in average monthly ITCZ width (degrees of latitude) between each respective GCM and GPCP observations, given as the model minus observations. Cells are shaded red (blue) in increasing intensity when the width of the ITCZ simulated by the GCM was found to be wider (thinner) compared to the GPCP ITCZ width.

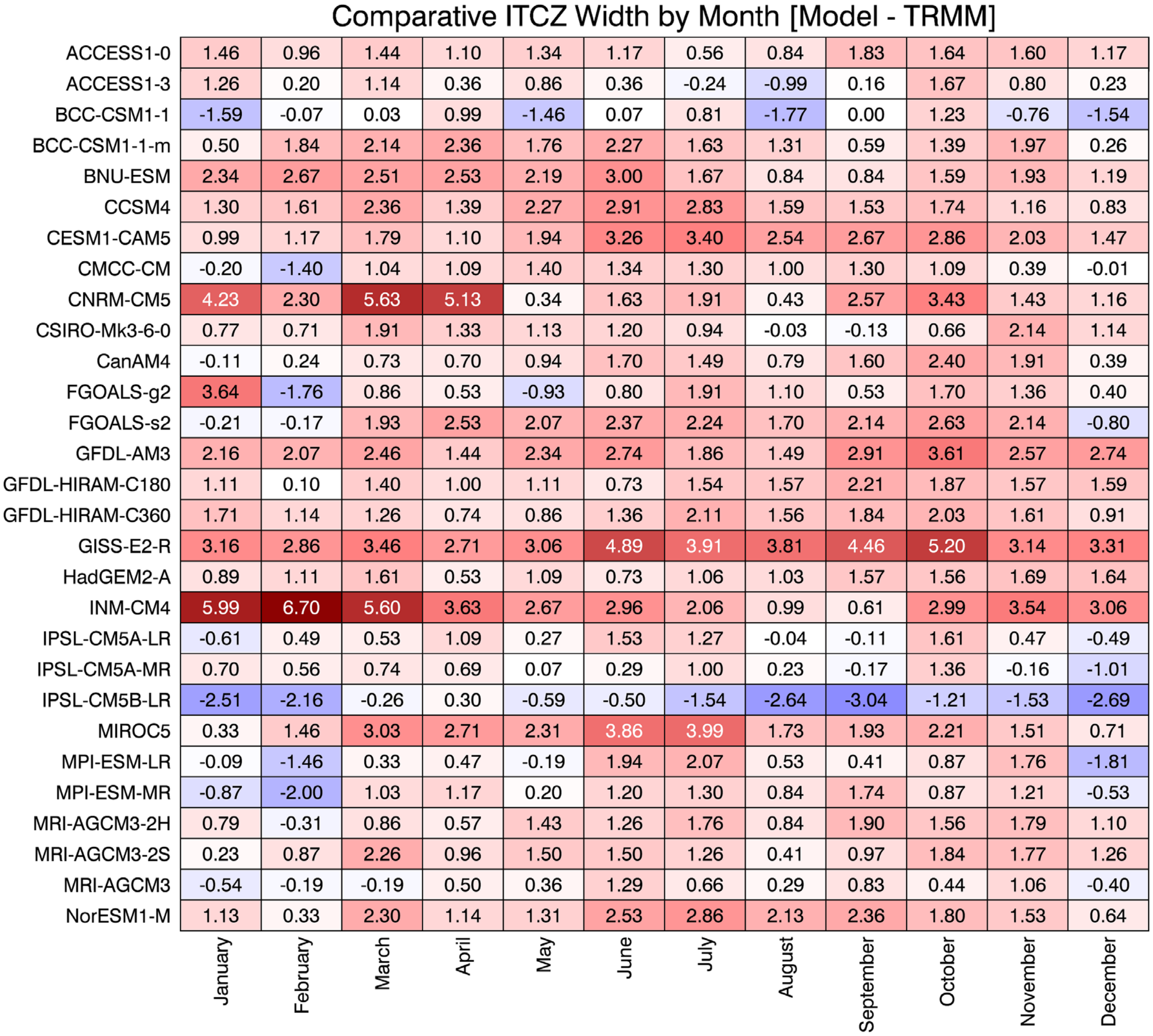

Comparative ITCZ Width by Month [Model - TRMM]

	January	February	March	April	May	June	July	August	September	October	November	December
ACCESS1-0	1.46	0.96	1.44	1.10	1.34	1.17	0.56	0.84	1.83	1.64	1.60	1.17
ACCESS1-3	1.26	0.20	1.14	0.36	0.86	0.36	-0.24	-0.99	0.16	1.67	0.80	0.23
BCC-CSM1-1	-1.59	-0.07	0.03	0.99	-1.46	0.07	0.81	-1.77	0.00	1.23	-0.76	-1.54
BCC-CSM1-1-m	0.50	1.84	2.14	2.36	1.76	2.27	1.63	1.31	0.59	1.39	1.97	0.26
BNU-ESM	2.34	2.67	2.51	2.53	2.19	3.00	1.67	0.84	0.84	1.59	1.93	1.19
CCSM4	1.30	1.61	2.36	1.39	2.27	2.91	2.83	1.59	1.53	1.74	1.16	0.83
CESM1-CAM5	0.99	1.17	1.79	1.10	1.94	3.26	3.40	2.54	2.67	2.86	2.03	1.47
CMCC-CM	-0.20	-1.40	1.04	1.09	1.40	1.34	1.30	1.00	1.30	1.09	0.39	-0.01
CNRM-CM5	4.23	2.30	5.63	5.13	0.34	1.63	1.91	0.43	2.57	3.43	1.43	1.16
CSIRO-Mk3-6-0	0.77	0.71	1.91	1.33	1.13	1.20	0.94	-0.03	-0.13	0.66	2.14	1.14
CanAM4	-0.11	0.24	0.73	0.70	0.94	1.70	1.49	0.79	1.60	2.40	1.91	0.39
FGOALS-g2	3.64	-1.76	0.86	0.53	-0.93	0.80	1.91	1.10	0.53	1.70	1.36	0.40
FGOALS-s2	-0.21	-0.17	1.93	2.53	2.07	2.37	2.24	1.70	2.14	2.63	2.14	-0.80
GFDL-AM3	2.16	2.07	2.46	1.44	2.34	2.74	1.86	1.49	2.91	3.61	2.57	2.74
GFDL-HIRAM-C180	1.11	0.10	1.40	1.00	1.11	0.73	1.54	1.57	2.21	1.87	1.57	1.59
GFDL-HIRAM-C360	1.71	1.14	1.26	0.74	0.86	1.36	2.11	1.56	1.84	2.03	1.61	0.91
GISS-E2-R	3.16	2.86	3.46	2.71	3.06	4.89	3.91	3.81	4.46	5.20	3.14	3.31
HadGEM2-A	0.89	1.11	1.61	0.53	1.09	0.73	1.06	1.03	1.57	1.56	1.69	1.64
INM-CM4	5.99	6.70	5.60	3.63	2.67	2.96	2.06	0.99	0.61	2.99	3.54	3.06
IPSL-CM5A-LR	-0.61	0.49	0.53	1.09	0.27	1.53	1.27	-0.04	-0.11	1.61	0.47	-0.49
IPSL-CM5A-MR	0.70	0.56	0.74	0.69	0.07	0.29	1.00	0.23	-0.17	1.36	-0.16	-1.01
IPSL-CM5B-LR	-2.51	-2.16	-0.26	0.30	-0.59	-0.50	-1.54	-2.64	-3.04	-1.21	-1.53	-2.69
MIROC5	0.33	1.46	3.03	2.71	2.31	3.86	3.99	1.73	1.93	2.21	1.51	0.71
MPI-ESM-LR	-0.09	-1.46	0.33	0.47	-0.19	1.94	2.07	0.53	0.41	0.87	1.76	-1.81
MPI-ESM-MR	-0.87	-2.00	1.03	1.17	0.20	1.20	1.30	0.84	1.74	0.87	1.21	-0.53
MRI-AGCM3-2H	0.79	-0.31	0.86	0.57	1.43	1.26	1.76	0.84	1.90	1.56	1.79	1.10
MRI-AGCM3-2S	0.23	0.87	2.26	0.96	1.50	1.50	1.26	0.41	0.97	1.84	1.77	1.26
MRI-AGCM3	-0.54	-0.19	-0.19	0.50	0.36	1.29	0.66	0.29	0.83	0.44	1.06	-0.40
NorESM1-M	1.13	0.33	2.30	1.14	1.31	2.53	2.86	2.13	2.36	1.80	1.53	0.64

Supplemental Fig. C – Same as Fig. B but using TRMM observational results (Fig. 7b).

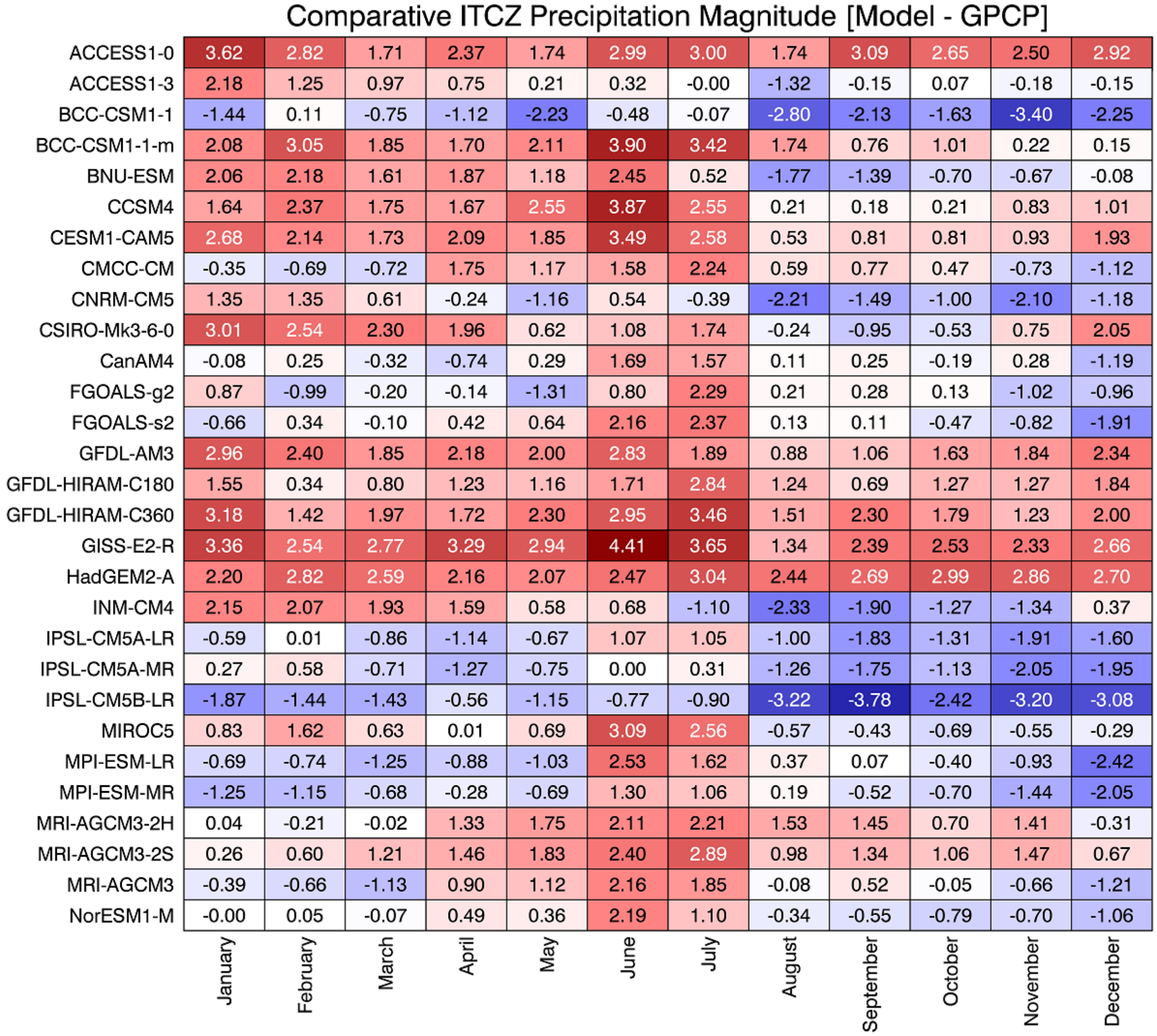

Comparative ITCZ Precipitation Magnitude [Model - GPCP]

	January	February	March	April	May	June	July	August	September	October	November	December
ACCESS1-0	3.62	2.82	1.71	2.37	1.74	2.99	3.00	1.74	3.09	2.65	2.50	2.92
ACCESS1-3	2.18	1.25	0.97	0.75	0.21	0.32	-0.00	-1.32	-0.15	0.07	-0.18	-0.15
BCC-CSM1-1	-1.44	0.11	-0.75	-1.12	-2.23	-0.48	-0.07	-2.80	-2.13	-1.63	-3.40	-2.25
BCC-CSM1-1-m	2.08	3.05	1.85	1.70	2.11	3.90	3.42	1.74	0.76	1.01	0.22	0.15
BNU-ESM	2.06	2.18	1.61	1.87	1.18	2.45	0.52	-1.77	-1.39	-0.70	-0.67	-0.08
CCSM4	1.64	2.37	1.75	1.67	2.55	3.87	2.55	0.21	0.18	0.21	0.83	1.01
CESM1-CAM5	2.68	2.14	1.73	2.09	1.85	3.49	2.58	0.53	0.81	0.81	0.93	1.93
CMCC-CM	-0.35	-0.69	-0.72	1.75	1.17	1.58	2.24	0.59	0.77	0.47	-0.73	-1.12
CNRM-CM5	1.35	1.35	0.61	-0.24	-1.16	0.54	-0.39	-2.21	-1.49	-1.00	-2.10	-1.18
CSIRO-Mk3-6-0	3.01	2.54	2.30	1.96	0.62	1.08	1.74	-0.24	-0.95	-0.53	0.75	2.05
CanAM4	-0.08	0.25	-0.32	-0.74	0.29	1.69	1.57	0.11	0.25	-0.19	0.28	-1.19
FGOALS-g2	0.87	-0.99	-0.20	-0.14	-1.31	0.80	2.29	0.21	0.28	0.13	-1.02	-0.96
FGOALS-s2	-0.66	0.34	-0.10	0.42	0.64	2.16	2.37	0.13	0.11	-0.47	-0.82	-1.91
GFDL-AM3	2.96	2.40	1.85	2.18	2.00	2.83	1.89	0.88	1.06	1.63	1.84	2.34
GFDL-HIRAM-C180	1.55	0.34	0.80	1.23	1.16	1.71	2.84	1.24	0.69	1.27	1.27	1.84
GFDL-HIRAM-C360	3.18	1.42	1.97	1.72	2.30	2.95	3.46	1.51	2.30	1.79	1.23	2.00
GISS-E2-R	3.36	2.54	2.77	3.29	2.94	4.41	3.65	1.34	2.39	2.53	2.33	2.66
HadGEM2-A	2.20	2.82	2.59	2.16	2.07	2.47	3.04	2.44	2.69	2.99	2.86	2.70
INM-CM4	2.15	2.07	1.93	1.59	0.58	0.68	-1.10	-2.33	-1.90	-1.27	-1.34	0.37
IPSL-CM5A-LR	-0.59	0.01	-0.86	-1.14	-0.67	1.07	1.05	-1.00	-1.83	-1.31	-1.91	-1.60
IPSL-CM5A-MR	0.27	0.58	-0.71	-1.27	-0.75	0.00	0.31	-1.26	-1.75	-1.13	-2.05	-1.95
IPSL-CM5B-LR	-1.87	-1.44	-1.43	-0.56	-1.15	-0.77	-0.90	-3.22	-3.78	-2.42	-3.20	-3.08
MIROC5	0.83	1.62	0.63	0.01	0.69	3.09	2.56	-0.57	-0.43	-0.69	-0.55	-0.29
MPI-ESM-LR	-0.69	-0.74	-1.25	-0.88	-1.03	2.53	1.62	0.37	0.07	-0.40	-0.93	-2.42
MPI-ESM-MR	-1.25	-1.15	-0.68	-0.28	-0.69	1.30	1.06	0.19	-0.52	-0.70	-1.44	-2.05
MRI-AGCM3-2H	0.04	-0.21	-0.02	1.33	1.75	2.11	2.21	1.53	1.45	0.70	1.41	-0.31
MRI-AGCM3-2S	0.26	0.60	1.21	1.46	1.83	2.40	2.89	0.98	1.34	1.06	1.47	0.67
MRI-AGCM3	-0.39	-0.66	-1.13	0.90	1.12	2.16	1.85	-0.08	0.52	-0.05	-0.66	-1.21
NorESM1-M	-0.00	0.05	-0.07	0.49	0.36	2.19	1.10	-0.34	-0.55	-0.79	-0.70	-1.06

Supplemental Fig. D – Table version of Figure 8a provided with quantitative values. Values in each cell depict the difference in precipitation (mm/day) between each GCM simulation and GPCP observation when averaged within ±4° latitude of the observed centerline, given as the model minus observations. Cells are shaded red (blue) in increasing intensity when the magnitude of precipitation in the GCM was found to be stronger (weaker) compared to the magnitude of precipitation within the GPCP ITCZ.

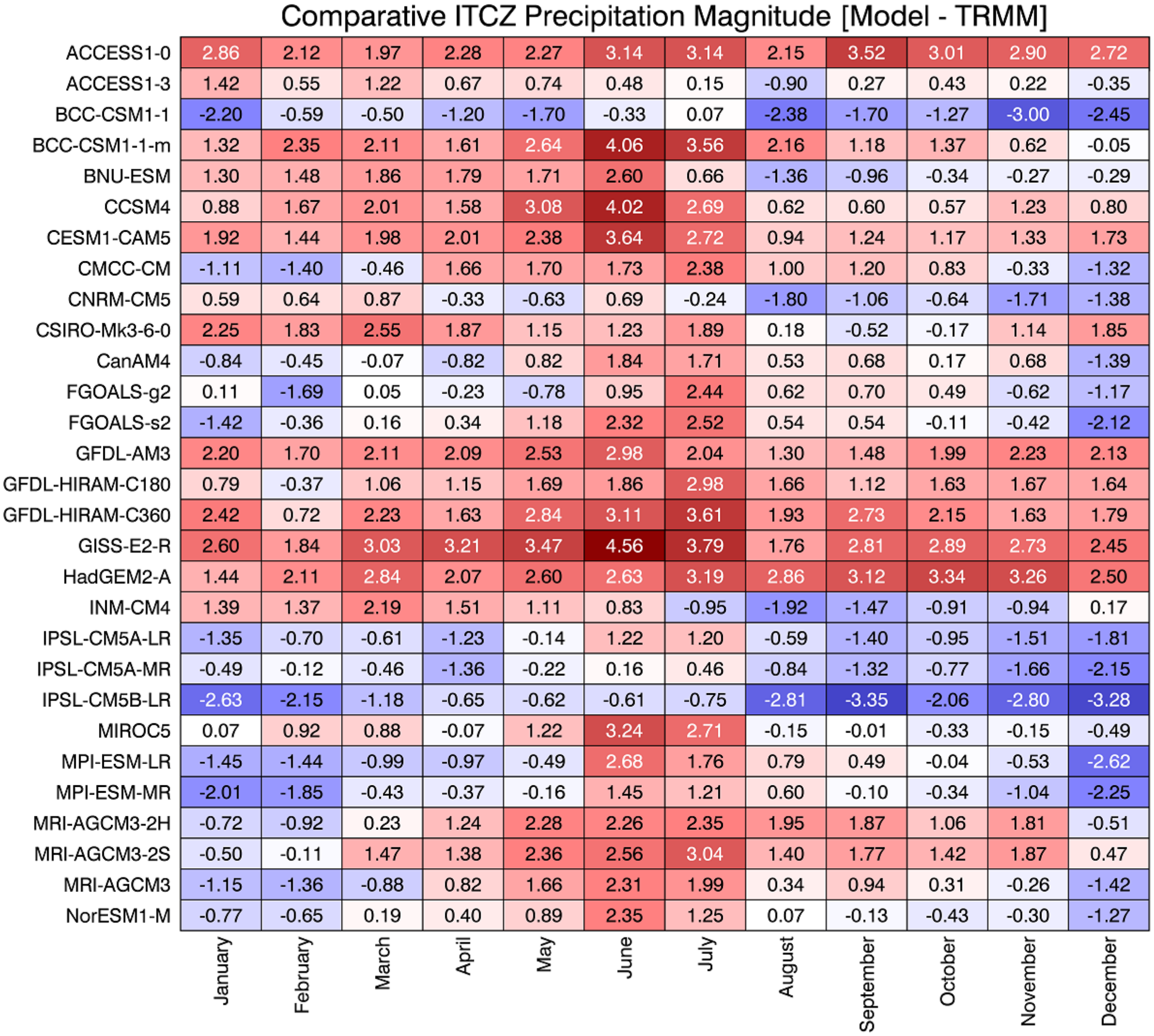

Comparative ITCZ Precipitation Magnitude [Model - TRMM]

	January	February	March	April	May	June	July	August	September	October	November	December
ACCESS1-0	2.86	2.12	1.97	2.28	2.27	3.14	3.14	2.15	3.52	3.01	2.90	2.72
ACCESS1-3	1.42	0.55	1.22	0.67	0.74	0.48	0.15	-0.90	0.27	0.43	0.22	-0.35
BCC-CSM1-1	-2.20	-0.59	-0.50	-1.20	-1.70	-0.33	0.07	-2.38	-1.70	-1.27	-3.00	-2.45
BCC-CSM1-1-m	1.32	2.35	2.11	1.61	2.64	4.06	3.56	2.16	1.18	1.37	0.62	-0.05
BNU-ESM	1.30	1.48	1.86	1.79	1.71	2.60	0.66	-1.36	-0.96	-0.34	-0.27	-0.29
CCSM4	0.88	1.67	2.01	1.58	3.08	4.02	2.69	0.62	0.60	0.57	1.23	0.80
CESM1-CAM5	1.92	1.44	1.98	2.01	2.38	3.64	2.72	0.94	1.24	1.17	1.33	1.73
CMCC-CM	-1.11	-1.40	-0.46	1.66	1.70	1.73	2.38	1.00	1.20	0.83	-0.33	-1.32
CNRM-CM5	0.59	0.64	0.87	-0.33	-0.63	0.69	-0.24	-1.80	-1.06	-0.64	-1.71	-1.38
CSIRO-Mk3-6-0	2.25	1.83	2.55	1.87	1.15	1.23	1.89	0.18	-0.52	-0.17	1.14	1.85
CanAM4	-0.84	-0.45	-0.07	-0.82	0.82	1.84	1.71	0.53	0.68	0.17	0.68	-1.39
FGOALS-g2	0.11	-1.69	0.05	-0.23	-0.78	0.95	2.44	0.62	0.70	0.49	-0.62	-1.17
FGOALS-s2	-1.42	-0.36	0.16	0.34	1.18	2.32	2.52	0.54	0.54	-0.11	-0.42	-2.12
GFDL-AM3	2.20	1.70	2.11	2.09	2.53	2.98	2.04	1.30	1.48	1.99	2.23	2.13
GFDL-HIRAM-C180	0.79	-0.37	1.06	1.15	1.69	1.86	2.98	1.66	1.12	1.63	1.67	1.64
GFDL-HIRAM-C360	2.42	0.72	2.23	1.63	2.84	3.11	3.61	1.93	2.73	2.15	1.63	1.79
GISS-E2-R	2.60	1.84	3.03	3.21	3.47	4.56	3.79	1.76	2.81	2.89	2.73	2.45
HadGEM2-A	1.44	2.11	2.84	2.07	2.60	2.63	3.19	2.86	3.12	3.34	3.26	2.50
INM-CM4	1.39	1.37	2.19	1.51	1.11	0.83	-0.95	-1.92	-1.47	-0.91	-0.94	0.17
IPSL-CM5A-LR	-1.35	-0.70	-0.61	-1.23	-0.14	1.22	1.20	-0.59	-1.40	-0.95	-1.51	-1.81
IPSL-CM5A-MR	-0.49	-0.12	-0.46	-1.36	-0.22	0.16	0.46	-0.84	-1.32	-0.77	-1.66	-2.15
IPSL-CM5B-LR	-2.63	-2.15	-1.18	-0.65	-0.62	-0.61	-0.75	-2.81	-3.35	-2.06	-2.80	-3.28
MIROC5	0.07	0.92	0.88	-0.07	1.22	3.24	2.71	-0.15	-0.01	-0.33	-0.15	-0.49
MPI-ESM-LR	-1.45	-1.44	-0.99	-0.97	-0.49	2.68	1.76	0.79	0.49	-0.04	-0.53	-2.62
MPI-ESM-MR	-2.01	-1.85	-0.43	-0.37	-0.16	1.45	1.21	0.60	-0.10	-0.34	-1.04	-2.25
MRI-AGCM3-2H	-0.72	-0.92	0.23	1.24	2.28	2.26	2.35	1.95	1.87	1.06	1.81	-0.51
MRI-AGCM3-2S	-0.50	-0.11	1.47	1.38	2.36	2.56	3.04	1.40	1.77	1.42	1.87	0.47
MRI-AGCM3	-1.15	-1.36	-0.88	0.82	1.66	2.31	1.99	0.34	0.94	0.31	-0.26	-1.42
NorESM1-M	-0.77	-0.65	0.19	0.40	0.89	2.35	1.25	0.07	-0.13	-0.43	-0.30	-1.27

Supplemental Fig. E – Same as Fig. D but using TRMM observational results (Fig. 8b).

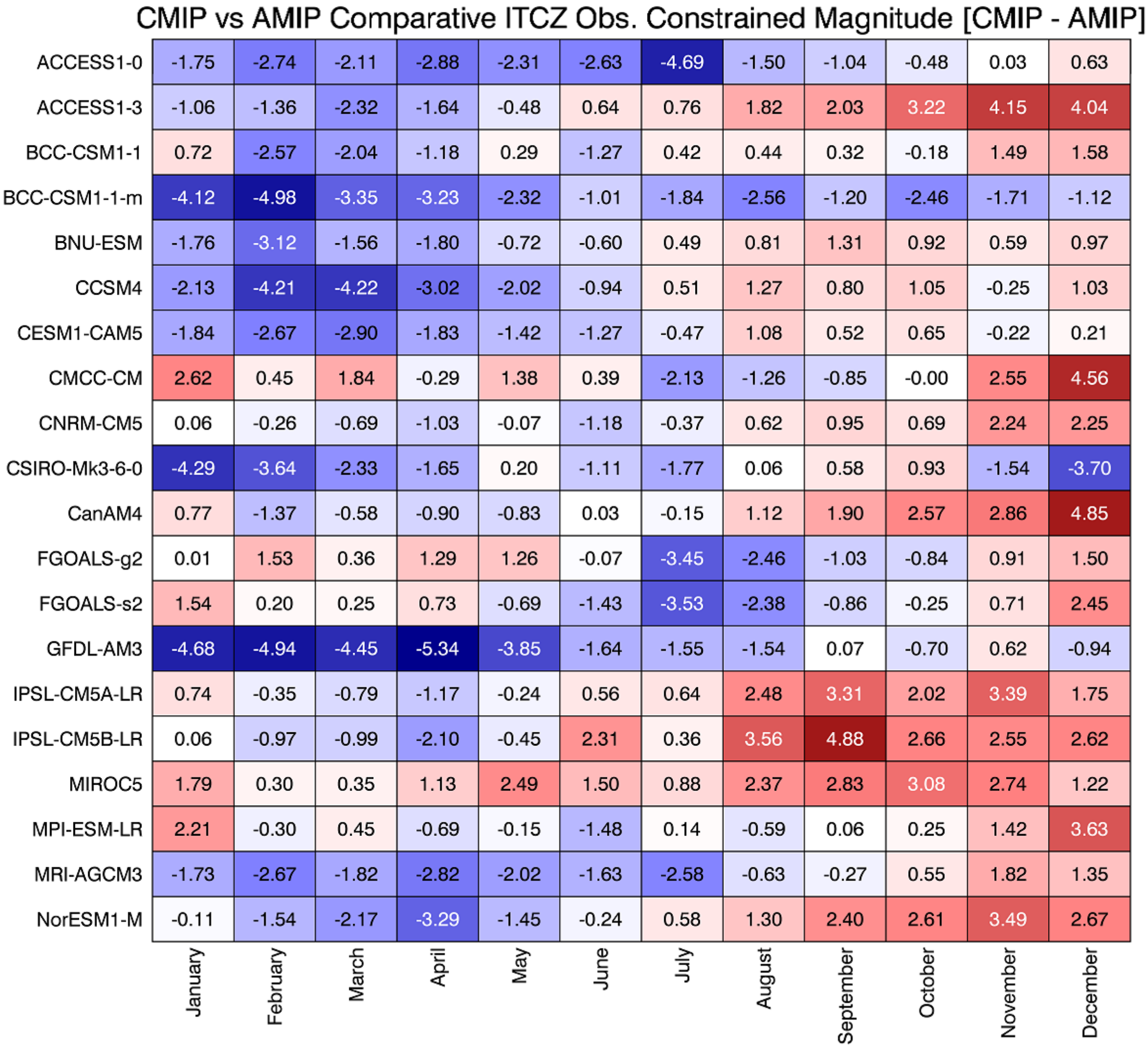

CMIP vs AMIP Comparative ITCZ Obs. Constrained Magnitude [CMIP - AMIP]

	January	February	March	April	May	June	July	August	September	October	November	December
ACCESS1-0	-1.75	-2.74	-2.11	-2.88	-2.31	-2.63	-4.69	-1.50	-1.04	-0.48	0.03	0.63
ACCESS1-3	-1.06	-1.36	-2.32	-1.64	-0.48	0.64	0.76	1.82	2.03	3.22	4.15	4.04
BCC-CSM1-1	0.72	-2.57	-2.04	-1.18	0.29	-1.27	0.42	0.44	0.32	-0.18	1.49	1.58
BCC-CSM1-1-m	-4.12	-4.98	-3.35	-3.23	-2.32	-1.01	-1.84	-2.56	-1.20	-2.46	-1.71	-1.12
BNU-ESM	-1.76	-3.12	-1.56	-1.80	-0.72	-0.60	0.49	0.81	1.31	0.92	0.59	0.97
CCSM4	-2.13	-4.21	-4.22	-3.02	-2.02	-0.94	0.51	1.27	0.80	1.05	-0.25	1.03
CESM1-CAM5	-1.84	-2.67	-2.90	-1.83	-1.42	-1.27	-0.47	1.08	0.52	0.65	-0.22	0.21
CMCC-CM	2.62	0.45	1.84	-0.29	1.38	0.39	-2.13	-1.26	-0.85	-0.00	2.55	4.56
CNRM-CM5	0.06	-0.26	-0.69	-1.03	-0.07	-1.18	-0.37	0.62	0.95	0.69	2.24	2.25
CSIRO-Mk3-6-0	-4.29	-3.64	-2.33	-1.65	0.20	-1.11	-1.77	0.06	0.58	0.93	-1.54	-3.70
CanAM4	0.77	-1.37	-0.58	-0.90	-0.83	0.03	-0.15	1.12	1.90	2.57	2.86	4.85
FGOALS-g2	0.01	1.53	0.36	1.29	1.26	-0.07	-3.45	-2.46	-1.03	-0.84	0.91	1.50
FGOALS-s2	1.54	0.20	0.25	0.73	-0.69	-1.43	-3.53	-2.38	-0.86	-0.25	0.71	2.45
GFDL-AM3	-4.68	-4.94	-4.45	-5.34	-3.85	-1.64	-1.55	-1.54	0.07	-0.70	0.62	-0.94
IPSL-CM5A-LR	0.74	-0.35	-0.79	-1.17	-0.24	0.56	0.64	2.48	3.31	2.02	3.39	1.75
IPSL-CM5B-LR	0.06	-0.97	-0.99	-2.10	-0.45	2.31	0.36	3.56	4.88	2.66	2.55	2.62
MIROC5	1.79	0.30	0.35	1.13	2.49	1.50	0.88	2.37	2.83	3.08	2.74	1.22
MPI-ESM-LR	2.21	-0.30	0.45	-0.69	-0.15	-1.48	0.14	-0.59	0.06	0.25	1.42	3.63
MRI-AGCM3	-1.73	-2.67	-1.82	-2.82	-2.02	-1.63	-2.58	-0.63	-0.27	0.55	1.82	1.35
NorESM1-M	-0.11	-1.54	-2.17	-3.29	-1.45	-0.24	0.58	1.30	2.40	2.61	3.49	2.67

Supplemental Fig. F - Table version of Fig. 9 provided with quantitative values. Values in each cell depict the differences in precipitation (mm/day) between CMIP and AMIP simulations when averaged within ±4° latitude of the observed centerline, given as CMIP minus AMIP. Cells are shaded red (blue) in increasing intensity when the magnitude of precipitation in the CMIP version of the GCM was found to be stronger (weaker) compared to its AMIP counterpart.